





Quantum density estimation with density matrices: Application to quantum anomaly detection

Diego H. Useche ^{*}, Oscar A. Bustos-Brinez , Joseph A. Gallego-Mejia , and Fabio A. González [†]
MindLab Research Group, Universidad Nacional de Colombia, 111321, Bogotá, Colombia

(Dated: March 19, 2024)

Density estimation is a central task in statistics and machine learning. This problem aims to determine the underlying probability density function that best aligns with an observed data set. Some of its applications include statistical inference, unsupervised learning, and anomaly detection. Despite its relevance, few works have explored the application of quantum computing to density estimation. In this article, we present a novel quantum-classical density matrix density estimation model, called Q-DEMDE, based on the expected values of density matrices and a novel quantum embedding called quantum Fourier features. The method uses quantum hardware to build probability distributions of training data via mixed quantum states. As a core subroutine, we propose a new algorithm to estimate the expected value of a mixed density matrix from its spectral decomposition on a quantum computer. In addition, we present an application of the method for quantum-classical anomaly detection. We evaluated the density estimation model with quantum random and quantum adaptive Fourier features on different data sets on a quantum simulator and a real quantum computer. An important result of this work is to show that it is possible to perform density estimation and anomaly detection with high performance on present-day quantum computers.

I. INTRODUCTION

Density estimation (DE) is an important problem in machine learning and statistics, which consists of determining the probability density function $p(\mathbf{x})$ of a set of data samples drawn from an unknown probability distribution. It is central to many areas of machine learning, including generative modeling [1], anomaly detection [2, 3], supervised classification [4] and clustering [5, 6]. Among its many applications include medical image analysis [7], epidemic policy [8], and urban planning [9]. An important area of application of DE is anomaly detection (AD), which aims to detect anomalous data that deviate from normal data. As an example, it can be applied to credit card fraud detection [10], where fraudulent transactions are seen as anomalies among normal transactions.

Density estimation can be addressed using parametric [11–13] and non-parametric methods [14–16]. Parametric density estimation aims to adjust the observed data to a prior probability distribution $p(\mathbf{x}|\boldsymbol{\theta})$, for instance, it may search for the parameters $\boldsymbol{\theta}$ that fit the data with a Gaussian distribution. By contrast, non-parametric methods such as kernel density estimation (KDE) [14, 15], do not assume a particular form of the distribution and they are therefore more flexible by reproducing arbitrary probability distributions. However, they are computationally expensive because they require storing in memory the whole data set.

Methods for density estimation have been widely addressed in classical computers [11, 14–16]; however, there are only a handful of works that explore the use of quantum computers for DE, including both parametric

[17, 18] and non-parametric methods [19, 20], of which some claim quantum advantage [18].

This recent enthusiasm for quantum computing has its roots in various theoretical works that illustrate that quantum computers may reduce the computational complexity of some classically-intractable problems [21, 22]. Nevertheless, today’s quantum hardware has not reached its full potential and it is prone to quantum noise [23, 24], hence some works have focused on building quantum machine learning algorithms [25, 26] for present-day quantum computers.

In this article, we present a novel non-parametric quantum-classical density matrix density estimation strategy, called Q-DEMDE, suitable for current noisy quantum computers. It combines a proposed quantum algorithm for computing the expectation values of density matrices with a novel quantum representation of data called quantum Fourier features. The proposed method, unlike previous quantum density estimation methods [19, 20], builds probability distributions of data in the form of mixed quantum states in qubit-based quantum hardware. It is based on the density matrix kernel density estimation (DMKDE) algorithm [27] originally developed for classical computers; it fuses density matrices with random Fourier features (RFF) [28] to build a non-parametric density estimator. We show that the proposed Q-DEMDE method can be implemented in current IBM quantum computers.

As an important quantum subroutine, we present a quantum algorithm, called Q-DMKDE, which estimates the expected value of a mixed density matrix in a quantum computer; this protocol extends to qubits a previous algorithm that performs the same operation in a high-dimensional quantum computer [19]. In contrast to pure-state classical sampling [29, 30], or methods like quantum state tomography [31], which build a density matrix in terms of the Pauli matrices, the proposed protocol pre-

^{*} diusecher@unal.edu.co

[†] fagonzalezo@unal.edu.co

compares a density matrix in a quantum computer from its spectral decomposition. In addition, we propose a randomized quantum map called quantum random Fourier features (QRFF) and a quantum variational mapping called quantum adaptive Fourier features (QAFF). These methods are analogous to RFF [28] and adaptive Fourier features (AFF) [32] respectively, and they are suitable for both classical and quantum computers; they represent classical data as quantum states, where the squared modulus of the inner product in the Hilbert space approximates a Gaussian kernel in the original space. We show that the Q-DEMDE method, which combines the QRFF and QAFF with the Q-DMKDE algorithm, allows us to perform quantum-classical density estimation (QDE) with a low number of qubits in both a quantum simulator and a real noisy quantum computer. Furthermore, we present a quantum-classical anomaly detection (QAD) strategy based on the proposed QDE method. We show that it is possible to perform both quantum density estimation and anomaly detection on current IBM quantum devices. In summary, the contributions of the article are as follows:

- (i) Two new quantum feature mappings called QRFF and QAFF, which can be viewed as quantum analogues of RFF [28] and AFF [32].
- (ii) An innovative quantum algorithm that estimates the expected value of a density matrix from its eigendecomposition.
- (iii) A quantum-classical density estimation method for current qubit-based quantum hardware that combines quantum Fourier features and quantum algorithms for expected value estimation.
- (iv) A quantum-classical anomaly detection strategy built on the proposed quantum-classical density estimation approach.

The structure of the document is as follows: in Sect. II, we describe the related work, in Sect. III, we present the theoretical background of the DMKDE algorithm and the notation for the description of the quantum circuits, in Sect. IV, we introduce our proposed Q-DEMDE method, outline the proposed Q-DMKDE protocol, and show the proposed QRFF and QAFF, in Sect. V, we present the results of our proposed method for quantum-classical density estimation, in Sect. VI we illustrate the application of the method for quantum-classical anomaly detection, and in Sect. VII we establish our conclusions and future outlook.

II. RELATED WORK

Density estimation is an important challenge in both classical and quantum machine learning. Both parametric and non-parametric methods for DE have been widely explored in classical computers [11–16, 27]. Some early

works on quantum density estimation build parametric models based on multivariate Gaussian distributions on quantum devices [17, 18]. On the non-parametric side, it is possible to combine the formalism of density matrices and kernels for density estimation as in the classical algorithms of kernel density matrices (KDM) [33] and DMKDE [27]; the latter combining density matrices with random Fourier features. Although DMKDE was originally developed for classical computers, it can be implemented in quantum computers with both pure-state and mixed-state approaches; the pure-state approach has been developed in qubit-based quantum computers [20], while the mixed-state version has been implemented in a high-dimensional quantum computer [19]. In contrast to these previous works, we present a QDE strategy built on mixed states for present-day qubit-based quantum devices and propose a quantum algorithm for estimating the expected value of a density matrix that extends the mixed-state DMKDE [19] to qubit-based quantum hardware.

Other quantum machine learning models based on mixed states include quantum support vector machines [34] and other kernel-based methods [29, 30, 35, 36]. These models require the preparation of mixed quantum states in quantum computers by building a purification of the mixed-state [34, 37], or by classically sampling the pure states that form the ensemble [29, 30]. In addition, it is possible to build a density matrix in the Pauli basis, like in the variational quantum eigensolver [38], and quantum state tomography [31, 39, 40], and using the density matrix exponentiation method [21], which prepares an exponential form of the density matrix by a unitary transformation, in analogy with the hamiltonian as the generator of time evolution. Our method differs from the previous techniques by preparing a density matrix for expected value estimation from its spectral decomposition.

González et. al. [41] proposed the use of random Fourier features (RFF) [28] as quantum feature maps. RFF approximates shift-invariant kernels by calculating an explicit mapping to a low-dimensional feature space. Improving the power of random Fourier features to approximate shift-invariant kernels is an active area of research. Two of the main approaches to the problem include refining the original RFF Monte Carlo sampling in either classical [42–44] or quantum computers [45] and using optimization techniques to find the optimal Fourier parameters [46, 47]. Among the methods that rely on optimization, adaptive Fourier features (AFF) [32] uses a siamese neural network to look for the optimal Fourier weights which reduce the mean squared distance between the Gaussian kernel and its Fourier feature approximation.

In this document, we present quantum random Fourier features, a randomized quantum feature map based on RFF [28], which induces a Gaussian kernel between data samples. In contrast to conventional RFF which builds an embedding in the real domain whose inner product ap-

proximates shift-invariant kernels, QRFF uses the complex form of RFF to approximate the kernel through the squared modulus of Hilbert inner product of the quantum features. Furthermore, we propose quantum adaptive Fourier features, a quantum variational method analogous to AFF suitable for both classical and quantum hardware. Previous works [48, 49] have shown that quantum mappings in the Fourier basis can be used to build models that are universal function approximators. In addition, it is also possible to use coherent states as quantum maps to induce Gaussian kernels [50]. The proposed QAFF method learns the frequencies of the QRFF using a strategy based on optimization, which in contrast to most quantum feature maps [49, 51, 52], allows to learn the optimal quantum embedding.

III. PRELIMINARIES

A. Kernel density estimation

Kernel density estimation, also called the Parzen-Rosenblat window [14, 15], is a non-parametric method for density estimation. Given a training data set, $\{\mathbf{x}_j\} \in \mathbb{R}^D$ and a kernel, the method builds a density estimator of a new test sample $\mathbf{x}^* \in \mathbb{R}^D$ by computing the kernel between all elements in the training data set and the test sample. Considering a Gaussian kernel $k(\mathbf{x}_j, \mathbf{x}^*) = e^{-\gamma\|\mathbf{x}_j - \mathbf{x}^*\|^2}$, where γ (gamma) is a parameter associated to the bandwidth, the probability density of the test sample \mathbf{x}^* is given by,

$$p_\gamma(\mathbf{x}^*) = \frac{1}{NM_\gamma} \sum_{j=0}^{N-1} k(\mathbf{x}_j, \mathbf{x}^*) = \frac{1}{NM_\gamma} \sum_{j=0}^{N-1} e^{-\gamma\|\mathbf{x}_j - \mathbf{x}^*\|^2}, \quad (1)$$

where $M_\gamma = (\pi/\gamma)^{\frac{D}{2}}$ is a normalization constant. This method scales with the size of the training data set and requires storing the whole data set in memory.

B. Random and Adaptive Fourier features

Random Fourier features [28], is a method that maps the space of characteristics $\mathbf{x} \in \mathbb{R}^D$ to a feature space $\mathbf{z}(\mathbf{x}) \in \mathbb{R}^d$ whose inner product approximates a shift-invariant kernel in the original space, i.e., $\mathbf{z}(\mathbf{x})^T \mathbf{z}(\mathbf{y}) \approx k(\mathbf{x} - \mathbf{y})$ for all $\mathbf{x}, \mathbf{y} \in \mathbb{R}^D$. For the case of the Gaussian kernel $k(\mathbf{x}, \mathbf{y}) = e^{-\gamma\|\mathbf{x} - \mathbf{y}\|^2}$, it builds a d -dimensional vector with parameter γ whose i^{th} component is given by,

$$\mathbf{z}_{\gamma,i}(\mathbf{x}) = \sqrt{\frac{2}{d}} \cos(\sqrt{2\gamma} \mathbf{w}_i \cdot \mathbf{x} + b_i) \quad (2)$$

by sampling i.i.d the weights $\{\mathbf{w}_i\} \in \mathbb{R}^D$ from $\mathcal{N}(\mathbf{0}, \mathbf{I})$, and i.i.d. biases $\{b_i\} \in \mathbb{R}$ from Uniform $[0, 2\pi]$, leading to $\mathbf{z}_\gamma(\mathbf{x})^T \mathbf{z}_\gamma(\mathbf{y}) \approx e^{-\gamma\|\mathbf{x} - \mathbf{y}\|^2}$. This method follows

from Bochner theorem [53], which states that a shift-invariant kernel is the Fourier transform of a probability measure, e.g., the Gaussian kernel with parameter γ is the Fourier transform of a normal distribution with variance 2γ . In addition, the kernel approximation can be improved by means of adaptive Fourier features [32], which learns the optimal RFF weights and biases $\{(\mathbf{w}_i, b_i)\}$ by minimizing the loss function, $\mathcal{L}_{\{(\mathbf{w}_i, b_i)\}} = \sum_{l,m} (k(\mathbf{x}_l, \mathbf{x}_m) - \mathbf{z}_\gamma(\mathbf{x}_l)^T \mathbf{z}_\gamma(\mathbf{x}_m))^2$, that reduces the distance between the kernel values of the samples in the data set and their Fourier feature approximation.

Furthermore, Ref. [27] showed that it is possible to build a quantum mapping by normalizing the RFF in the form,

$$|\bar{\psi}(\mathbf{x})\rangle = \frac{1}{\mathcal{N}} \sum_{i=0}^{d-1} \mathbf{z}_{\gamma/2,i}(\mathbf{x}) |i\rangle, \quad (3)$$

where, $\mathcal{N} = \|\mathbf{z}_{\gamma/2}(\mathbf{x})\|$, and the Fourier components constructed with parameter $\gamma/2$; it approximates the Gaussian kernel via $\langle \bar{\psi}(\mathbf{x}) | \bar{\psi}(\mathbf{y}) \rangle^2 \approx e^{-\gamma\|\mathbf{x} - \mathbf{y}\|^2}$ where $|\bar{\psi}(\mathbf{x})\rangle \in \mathbb{R}^d$.

In this article, we propose the quantum random and quantum adaptive Fourier features, which map the space of the characteristics $\mathbf{x} \in \mathbb{R}^D$, to a complex Hilbert space $|\psi(\mathbf{x})\rangle \in \mathbb{C}^d$, where the square of the modulus approximates the Gaussian kernel $|\langle \psi(\mathbf{x}) | \psi(\mathbf{y}) \rangle|^2 \approx e^{-\gamma\|\mathbf{x} - \mathbf{y}\|^2}$, see Sect. IV A. For notational purposes, we use a bar to distinguish the quantum map based on RFF in the real domain $|\bar{\psi}(\mathbf{x})\rangle$ from the quantum random and quantum adaptive Fourier features $|\psi(\mathbf{x})\rangle$.

C. Density matrix kernel density estimation

The machine learning algorithm density matrix kernel density estimation (DMKDE) [27] is a non-parametric method for density estimation which combines density matrices and random Fourier features [28], it does not require optimization and it works as an efficient approximation of kernel density estimation [14, 15].

The DMKDE method [27] starts by applying a quantum feature map based on RFF, see Eq. 3, to each sample in the train data set $\{\mathbf{x}_j\} \rightarrow \{|\bar{\psi}(\mathbf{x}_j)\rangle\}$, and to the test sample whose density we aim to estimate $\mathbf{x}^* \rightarrow |\bar{\psi}(\mathbf{x}^*)\rangle$, where $\mathbf{x} \in \mathbb{R}^D$ and $|\bar{\psi}(\mathbf{x})\rangle \in \mathbb{R}^d$.

Once the Fourier feature map is established, the method builds a training density matrix. For the training states $\{|\bar{\psi}(\mathbf{x}_j)\rangle\}_{j=0, \dots, N-1}$, the training mixed state is constructed by,

$$\bar{\rho}_{\text{train}} = \frac{1}{N} \sum_{j=0}^{N-1} |\bar{\psi}(\mathbf{x}_j)\rangle \langle \bar{\psi}(\mathbf{x}_j)|, \quad (4)$$

and the probability density of the testing sample $\mathbf{x}^* \rightarrow |\bar{\psi}(\mathbf{x}^*)\rangle$ is computed by,

$$\hat{p}_\gamma(\mathbf{x}^*) = \frac{1}{M_\gamma} \langle \bar{\psi}(\mathbf{x}^*) | \bar{\rho}_{\text{train}} | \bar{\psi}(\mathbf{x}^*) \rangle. \quad (5)$$

The complexity of the prediction phase of the DMKDE algorithm is $O(d^2)$, which is independent of the size of the training data. Furthermore, by replacing Eq. 4 on Eq. 5, we obtain,

$$\begin{aligned} \hat{p}_\gamma(\mathbf{x}^*) &= \frac{1}{M_\gamma} \langle \bar{\psi}(\mathbf{x}^*) | \left(\frac{1}{N} \sum_{j=0}^{N-1} |\bar{\psi}(\mathbf{x}_j)\rangle \langle \bar{\psi}(\mathbf{x}_j)| \right) | \bar{\psi}(\mathbf{x}^*) \rangle \\ &= \frac{1}{NM_\gamma} \sum_{j=0}^{N-1} |\langle \bar{\psi}(\mathbf{x}_j) | \bar{\psi}(\mathbf{x}^*) \rangle|^2 \\ &\approx \frac{1}{NM_\gamma} \sum_{j=0}^{N-1} e^{-\gamma \|\mathbf{x}_j - \mathbf{x}^*\|^2} = p_\gamma(\mathbf{x}^*). \end{aligned} \quad (6)$$

Hence, $\hat{p}_\gamma(\mathbf{x}^*)$ as defined above converges to the Gaussian kernel density estimator $p_\gamma(\mathbf{x}^*)$. The following proposition from Ref. [27] illustrates the precision of the approximation.

Proposition 1 (González et. al. [27]) *Let \mathcal{M} be a compact subset of \mathbb{R}^D with diameter $\text{diam}(\mathcal{M})$, let $X = \{\mathbf{x}_i\}_{i=0, \dots, N-1} \subset \mathcal{M}$ a set of i.i.d samples, then \hat{p}_γ and p_γ (Eq. 6) satisfy:*

$$\Pr \left[\sup_{\mathbf{x} \in \mathcal{M}} |\hat{p}_\gamma(\mathbf{x}) - p_\gamma(\mathbf{x})| \geq \epsilon \right] \leq 2^8 \left(\frac{\sqrt{2D\gamma} \text{diam}(\mathcal{M})}{3M_\gamma \epsilon} \right) \exp \left(-\frac{d(3M_\gamma \epsilon)^2}{4(D+2)} \right) \quad (7)$$

Thus, the DMKDE algorithm as an approximation of the KDE method [14, 15] can be improved by increasing the number of Fourier features d . This approximation has the advantage of reducing the computational complexity, since for M samples, the DMKDE algorithm combined with RFF reduces the number of operations of the Parzen-Rosenblatt window from $O(NM)$ to $O(M+N)$, see Sect. IV D, and its complexity does not grow exponentially with the size D of the data, in contrast to the fast multipole method for KDE [54–56].

In addition, Eqs. 4, 5, and 6 can be extended to our proposed Q-DEMDE method, see Sect. IV, which combines a quantum implementation of the DMKDE with quantum random and quantum adaptive Fourier features for density estimation; the precision of the density estimation method (Eq. 7) also applies to the Q-DEMDE method with QRFF.

D. Notation for the quantum circuits

We now introduce the notation of the quantum circuits used in the article, which is the same notation as in Ref. [57]. Each state of the canonical basis of an n -qubit state can be written as $|b_0 b_1 \dots b_{n-1}\rangle$ with $\{b_i\} \in \{0, 1\}$, hence, we may write any state in the canonical basis as a string in its binary form. This notation can be simplified by writing such state as $\left| \sum_{i=0}^{n-1} b_i 2^i \right\rangle_n$, namely, the bit string

is written in decimal form and the subindex indicates the number of qubits of the state. For example, the 4-qubit state $|1010\rangle$ can be written as $|5\rangle_4$. We use of the same subindex to emphasize the number of qubits that make up a quantum state preparation or a unitary transformation. For example, a quantum state of size 2^n and a unitary matrix of size $2^n \times 2^n$ can be built on n qubits and written as $|\psi\rangle_n$ and U_n , respectively.

E. Amplitude encoding, unitaries and isometries

Two key ingredients of the quantum algorithms presented in this article are quantum state preparation and isometries. Several quantum protocols have been proposed for quantum state preparation, also called amplitude encoding [58, 59]. The problem consists on the construction of an arbitrary quantum state $|\psi\rangle \in \mathbb{C}^d$ in a quantum computer. The protocol requires at least $n = \lceil \log(d) \rceil$ qubits and it allows to prepare the complex components of the state in the amplitudes of the basis of binary bit strings, in the form,

$$|\psi\rangle_n = \sum_{i=0}^{d-1} a_i |i\rangle_n, \quad (8)$$

where, $\{a_i\}$ are the complex amplitudes of the quantum state $|\psi\rangle$ and $\{|i\rangle_n\}$ is the binary basis for an n qubit state written in decimal form. The depth (number of CNOTs) of the circuit required to build an arbitrary quantum state scales exponentially [58, 59] with the number of qubits $O(2^n) = O(d)$.

The application of an arbitrary unitary transformation $U \in \mathbb{C}^{d \times d}$ on $n = \lceil \log(d) \rceil$ qubits is an important quantum subroutine, whose depth is of the order $O(d^2)$. Unitary transformations are a subset of a more general transformation called isometries [57], which correspond to transformations from two Hilbert spaces that may have different dimensions, say $\mathbb{C}^r \rightarrow \mathbb{C}^d$. An isometry from $m = \log(r)$ to $n = \log(d)$ qubits can be regarded as a $\mathbb{C}^{d \times r}$ transformation built from the first r columns of a $\mathbb{C}^{d \times d}$ unitary matrix; amplitude encoding can also be seen as an isometry with $r = 1$. Isometries are of particular interest because the circuit depth of isometries scales in the form $O(dr)$, which has lower complexity than arbitrary unitary transformations. Table I summarizes the number of qubits and circuit depth of amplitude encoding, unitary matrices, and isometries.

Subroutine	Dimension	Num. qubits	Circuit depth
State preparation	d	$\log(d)$	d
Unitary	$d \times d$	$\log(d)$	d^2
Isometry	$d \times r$	$\log(d)$	dr

TABLE I. Scale of the number of qubits and circuit depth (number of CNOTS) to build arbitrary quantum states, unitaries, and isometries.

IV. QUANTUM-CLASSICAL DENSITY MATRIX DENSITY ESTIMATION (Q-DEMDE)

We propose a quantum-classical density matrix-based density estimation model called Q-DEMDE based on a novel quantum implementation of the DMKDE algorithm [27], see Sect. III C, and the novel quantum random and quantum adaptive Fourier features. Fig. 1 shows the main steps of the Q-DEMDE method: (i) quantum feature map, (ii) training phase, and (iii) density estimation of new samples. Steps (i) and (ii) are calculated on a classical computer, while step (iii) is computed on a quantum computer. These steps are described in more detail below.

- (i) Quantum feature map: Apply a feature map based on QRFF or QAFF, see Sects. IV A and IV B, in a classical computer, to the training data set $\{\mathbf{x}_j\} \rightarrow \{|\psi(\mathbf{x}_j)\rangle\}$, and to the test sample $\mathbf{x}^* \rightarrow |\psi(\mathbf{x}^*)\rangle$, whose density with respect to the training data we want to estimate.
- (ii) Training phase: Use a classical computer to build the training density matrix $\rho_{\text{train}} = (1/N) \sum |\psi(\mathbf{x}_j)\rangle \langle\psi(\mathbf{x}_j)|$ from the training features, as in Eq. 4, and calculate its spectral decomposition, $\rho_{\text{train}} = V\Lambda V^\dagger$. The training mixed quantum state encodes a probability distribution of the training data set.
- (iii) Prediction phase: From the test quantum state and the spectral decomposition of training density matrix, use a quantum computer to estimate the probability density of the test sample by calculating the expectation value of the test state with the training density matrix, $M_\gamma^{-1} \langle\psi(\mathbf{x}^*)|\rho_{\text{train}}|\psi(\mathbf{x}^*)\rangle = M_\gamma^{-1} \langle\psi(\mathbf{x}^*)|V\Lambda V^\dagger|\psi(\mathbf{x}^*)\rangle$, as in Eq. 5, using the proposed Q-DMKDE quantum protocol shown in Fig. 4. See Sect. IV C for the mathematical details of this quantum algorithm.

In the following sections, we present the theoretical details of the new quantum Fourier features and the proposed Q-DMKDE quantum protocol, which estimates the expected value of an eigen-decomposed density matrix.

A. Quantum random Fourier features

To build the quantum features of the quantum density estimation method, we propose a novel embedding called quantum random Fourier features (QRFF), which correspond to RFF [28] in the complex domain. QRFF build a quantum feature map that approximates a Gaussian kernel by mapping classical data samples $\mathbf{x} \in \mathbb{R}^D$ to quantum state-like representations $|\psi(\mathbf{x})\rangle \in \mathbb{C}^d$, such that, $\hat{k}(\mathbf{x}, \mathbf{y}) = |\langle\psi(\mathbf{x})|\psi(\mathbf{y})\rangle|^2$ approximates $k(\mathbf{x}, \mathbf{y}) = e^{-\gamma\|\mathbf{x}-\mathbf{y}\|^2}$. The QRFF is distinct from conventional RFF

[28] by approximating the kernel via $|\langle\psi(\mathbf{x})|\psi(\mathbf{y})\rangle|^2$ instead of a dot product $\mathbf{z}_\gamma(\mathbf{x})^T \mathbf{z}_\gamma(\mathbf{y})$.

The proposed QRFF builds the following quantum mapping, which approximates a Gaussian kernel,

$$|\psi(\mathbf{x})\rangle = \sqrt{\frac{1}{d}} [e^{i\sqrt{\gamma}\mathbf{w}_0 \cdot \mathbf{x}}, e^{i\sqrt{\gamma}\mathbf{w}_1 \cdot \mathbf{x}}, \dots, e^{i\sqrt{\gamma}\mathbf{w}_{d-1} \cdot \mathbf{x}}]' \quad (9)$$

by sampling the i.i.d. weights $\{\mathbf{w}_j\} \in \mathbb{R}^D$ from $\mathcal{N}(\mathbf{0}, \mathbf{I}_D)$, where \mathbf{I}_D is the D -dimensional identity matrix. This method finds justification from Bochner theorem [53], which states that a continuous kernel $k(\mathbf{x} - \mathbf{y})$ on \mathbb{R}^D is positive definite if it is the Fourier transform of a non-negative measure. Extending the argument of Ref. [28] to the quantum domain, this theorem can be applied to the Fourier relation between position $\psi(\Delta)$ and momentum $\phi(\mathbf{p})$ wavefunctions, with $\Delta = \mathbf{x} - \mathbf{y}$, i.e., $\psi(\mathbf{x} - \mathbf{y}) = (2\pi)^{-(D/2)} \int_{\mathbb{R}^D} \phi(\mathbf{p}) e^{i\mathbf{p} \cdot (\mathbf{x} - \mathbf{y})} d\mathbf{p}$, the position wavefunction results from the inverse Fourier transform of the momentum wavefunction. Considering a Gaussian wavepacket $\phi(\mathbf{p}) = (\pi\gamma)^{-(D/4)} e^{-\|\mathbf{p}\|^2/(2\gamma)}$, we have that,

$$(\pi/\gamma)^{D/4} \psi(\mathbf{x} - \mathbf{y}) = \int_{\mathbb{R}^D} (2\pi\gamma)^{-(D/2)} e^{-\|\mathbf{p}\|^2/(2\gamma)} e^{i\mathbf{p} \cdot (\mathbf{x} - \mathbf{y})} d\mathbf{p}, \quad (10)$$

by writing the last integral as a sum, we have that, $E[e^{i\mathbf{p} \cdot \mathbf{x}} e^{-i\mathbf{p} \cdot \mathbf{y}}] \approx \langle\psi(\mathbf{y})|\psi(\mathbf{x})\rangle$ with $|\psi(\mathbf{x})\rangle = \sqrt{1/d} \sum_{j=0}^{d-1} e^{i\mathbf{p}_j \cdot \mathbf{x}} |j\rangle$ is an unbiased estimate of $(\pi/\gamma)^{D/4} \psi(\mathbf{x} - \mathbf{y})$, when $\{\mathbf{p}_j\}$ is sampled i.i.d. from $\mathcal{N}(\mathbf{0}, \gamma\mathbf{I}_D)$, since the term that complements the complex exponential in Eq. 10 is a multivariate Gaussian with mean $\mathbf{0}$ and covariance matrix $\gamma\mathbf{I}_D$. Therefore, we may build the Gaussian kernel by $k(\mathbf{x} - \mathbf{y}) = e^{-\gamma\|\mathbf{x}-\mathbf{y}\|^2} = (\pi/\gamma)^{D/2} \psi(\mathbf{x} - \mathbf{y})^* \psi(\mathbf{x} - \mathbf{y}) \approx |\langle\psi(\mathbf{x})|\psi(\mathbf{y})\rangle|^2$, considering that, $\psi(\mathbf{x} - \mathbf{y}) = (\gamma/\pi)^{D/4} e^{-\gamma\|\mathbf{x}-\mathbf{y}\|^2/2}$, for the Gaussian wavepacket in the position representation.

B. Quantum adaptive Fourier features

In analogy with adaptive Fourier features [32], we also propose quantum adaptive Fourier features (QAFF) which improves the Gaussian kernel approximation of QRFF. It uses optimization techniques to find the optimal parameters $\{\mathbf{w}_j\}$, from Eq. 9, by minimizing a loss function that reduces the distance between the actual kernel and its Fourier feature representation such as the mean square error loss function,

$$\mathcal{L}_{\{\mathbf{w}_j\}} = \frac{1}{T} \sum_{l=1}^{\mathcal{M}} \sum_{m=l}^{\mathcal{M}} (k(\mathbf{x}_l, \mathbf{x}_m) - \hat{k}_{\{\mathbf{w}_j\}}(\mathbf{x}_l, \mathbf{x}_m))^2, \quad (11)$$

where $\{\mathbf{x}_l\}_{1 \dots \mathcal{M}} \in \mathbb{R}^D$ is referred to as kernel training data set, which is written in italics to distinguish it from the training data set of the density estimation task

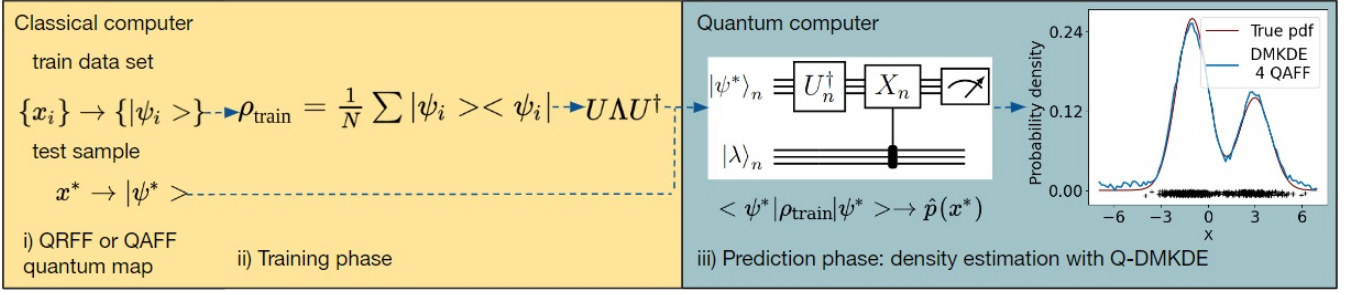


FIG. 1. Q-DEMDE method for quantum-classical density estimation with density matrices and quantum Fourier features. In step i) we perform the feature map based on QRFF or QAFF in a classical computer, in step ii) we construct the training density matrix with the training data and find its spectral decomposition using a classical computer, and finally in step iii) we find the density estimate of the test sample with the training density matrix in a quantum computer using the proposed Q-DMKDE quantum algorithm.

$\{\mathbf{x}_l\}_{1\dots N} \in \mathbb{R}^D$. Also, $\{(\mathbf{x}_l, \mathbf{x}_m)\}_{1\dots T}$, is called the set of all the data pairs of the kernel training data set, clearly, $T = \mathcal{M}(\mathcal{M} + 1)/2$.

To optimize the weights $\{\mathbf{w}_j\}$ of QAFF, we initialize randomly these parameters (we may use, for instance, the QRFF weights, however, its initialization is not restricted to them), and apply the usual gradient descend update rule,

$$\mathbf{w}_j^{(t+1)} = \mathbf{w}_j^{(t)} - \eta \nabla_{\mathbf{w}_j} \mathcal{L}_{\{\mathbf{w}_k\}}^{(t)}, \quad (12)$$

where η is the learning rate, and t is the time of the iteration.

To train the QAFF, we can use a siamese neural network to estimate $|\langle \psi(\mathbf{x}_l) | \psi(\mathbf{x}_m) \rangle|^2$ and to fit that value as close as possible to $e^{-\gamma \|\mathbf{x}_l - \mathbf{x}_m\|^2}$, as in conventional AFF [32], see Fig. 2 for its neural architecture, however, in the Appendix. B, we present an explicit mathematical expression of the gradient $\nabla_{\mathbf{w}_j} \mathcal{L}_{\{\mathbf{w}_k\}}$, which avoids the use of the siamese neural network, also showing that the complexity of training QAFF in a classical computer is $O(TdD + Td^2)$.

Once the appropriate weights $\{\mathbf{w}_k\}$ of the QAFF are learned, we apply the quantum Fourier map, see Eq. 9, to the training data set $\{\mathbf{x}_j\} \rightarrow \{|\psi(\mathbf{x}_j)\rangle\}$ and to the test sample $\mathbf{x}^* \rightarrow |\psi(\mathbf{x}^*)\rangle$ whose probability density we aim to estimate.

1. The kernel training data set to optimize the QAFF

One key element in the trainability of the quantum adaptive Fourier features is the kernel training data set $\{\mathbf{x}_l\}_{1\dots \mathcal{M}}$, and its data pairs $\{(\mathbf{x}_l, \mathbf{x}_m)\}_{1\dots T}$. In this section, we present two alternatives as kernel training data sets to train the QAFF.

The Gaussian kernel training data set: The main kernel training data set used in this article is the Gaussian data set. To approximate the Gaussian kernel $e^{-\gamma \|\mathbf{x}_l - \mathbf{x}_m\|^2}$, whose original space is $\mathbf{x} \in \mathbb{R}^D$, we build

a synthetic data set $\{\mathbf{x}_l\}_{1\dots \mathcal{M}}$ sampled from a multivariate normal distribution $\mathcal{N}(\mathbf{0}, \frac{1}{2\gamma D} \mathbf{I}_D)$. In addition, since the Gaussian kernel is shift-invariant, in this kernel training strategy we set one of the elements of each data pair equal to $\mathbf{0}$, so the new data pairs are $\{(\mathbf{x}_l, \mathbf{0})\}_{1\dots \mathcal{M}}$, and the loss function to optimize becomes $\mathcal{L}_{\{\mathbf{w}_j\}} = \frac{1}{\mathcal{M}} \sum_l (|\langle \psi(\mathbf{x}_l) | \psi(\mathbf{0}) \rangle|^2 - e^{-\gamma \|\mathbf{x}_l\|^2})^2$. The motivation of this kernel learning strategy is that the Gaussian data resulting from sampling $\mathcal{N}(\mathbf{0}, \frac{1}{2\gamma D} \mathbf{I}_D)$ is equivalent to sampling from the kernel function $e^{-\gamma \|\mathbf{x}\|^2}$, so there would be a greater number of kernel training points in the regions with larger values of the kernel function, leading to better approximation of the kernel in those regions. Furthermore, since γ acts as a scaling factor in this kernel learning strategy, the learned weights do not depend on γ , and we can simplify the method by setting $\gamma = 0.5$, nonetheless, when predicting the QAFF mapping on the training data set $\{\mathbf{x}_j\}_{1\dots N}$ and testing sample \mathbf{x}^* , which are distinct from the kernel training data samples, it is necessary to choose the appropriate γ value that approximates the desired kernel as in QRFF.

The ML problem kernel training data set: When solving a machine learning (ML) problem with training data points $\{\mathbf{x}_j\}_{1\dots N} \in \mathbb{R}^D$, one can use a subset of samples from training data set $\{\mathbf{x}_l\}_{1\dots \mathcal{M}} \subseteq \{\mathbf{x}_j\}_{1\dots N}$ to approximate the Gaussian kernel for the training data set. Namely, in this setting the loss function, see Eq. 11, is optimized using the data pairs $\{(\mathbf{x}_l, \mathbf{x}_m)\}_{1\dots T}$, which are samples from the original training data. This approach has been explored in conventional adaptive Fourier features [32], however, it does not guarantee an appropriate approximation of the kernel for some novel data that deviates from the training data of the ML problem.

2. Additional: Quantum variational circuit implementation of QAFF

Although the loss function of the proposed classical QAFF method can be trained with classical computers

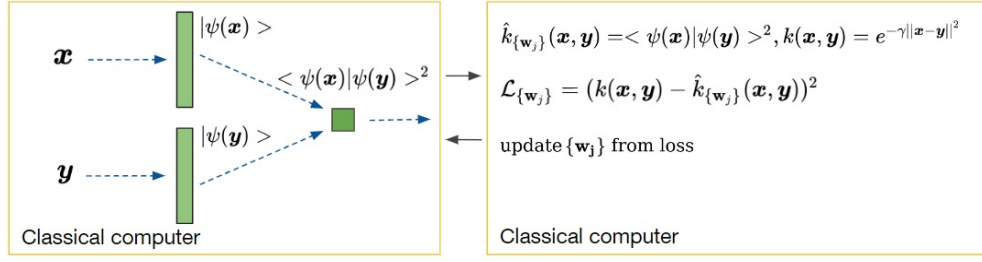


FIG. 2. Quantum adaptive Fourier features method for learning the Gaussian kernel in a classical computer. A Siamese neural network constructs the quantum Fourier map of the data pair $(\mathbf{x}, \mathbf{y}) \rightarrow (|\psi(\mathbf{x})\rangle, |\psi(\mathbf{y})\rangle)$, the weights of the feature map $\{\mathbf{w}_j\}$ are the same on both feature mappings and they are randomly initialized; these weights are learned by minimizing a loss function $\mathcal{L}_{\{\mathbf{w}_j\}}$ that reduces the distance between the Gaussian kernel and its Fourier feature approximation. To approximate the Gaussian kernel with QAFF, we explore two alternative kernel training data sets: the Gaussian kernel training data set and the ML kernel training data set, see Sect. IV B 1.

using siamese neural networks as in AFF [32] or by computing the gradient of the loss function, see Eq. B2, for completeness, we also present a quantum variational strategy to optimize in a quantum computer the loss function (Eq. 11) of the proposed QAFF method, see Fig. 3.

We show how to prepare in a quantum computer the QAFF mapping $|\psi(\mathbf{x})\rangle = \sqrt{\frac{1}{d}} [1, e^{i\sqrt{\gamma}\mathbf{w}_1 \cdot \mathbf{x}}, \dots, e^{i\sqrt{\gamma}\mathbf{w}_{d-1} \cdot \mathbf{x}}]'$, which learns variationally the optimal weights of the QRFF (note that the global phase might be ignored by setting $\mathbf{w}_0 = \mathbf{0}$). To prepare this $n = \log d$ qubit state, we may use a method based on amplitude encoding [58], it consists on applying the unitary $H^{\otimes n}$ on the initial $|0\rangle^{\otimes n}$ state which builds the quantum state $|+\rangle^{\otimes n}$, then it applies a series $d - 1$ of uniformly controlled $R_z(\alpha) = |0\rangle\langle 0| + e^{i\alpha}|1\rangle\langle 1|$ rotations with angles $\{\sqrt{\gamma}\mathbf{w}_j \cdot \mathbf{x}\}_{j=1, \dots, d-1}$, whose controls correspond to the first $n - 1$ qubits and its target corresponds to the n^{th} qubit, each k^{th} uniformly controlled rotation works by controlling a quantum state of the first $n - 1$ qubits corresponding to the bitstring $|b_0^k b_1^k \dots b_{n-2}^k\rangle$ with $\{b_i^k\} \in \{0, 1\}$ where the \circ symbol indicates a control on the $|0\rangle$ qubit state and the \bullet symbol indicates a control on the $|1\rangle$ qubit state, as shown in Fig. 3b. By writing the bit string in decimal form $|b_0^k b_1^k \dots b_{n-2}^k\rangle = |k \pmod{(d/2)}\rangle_{n-1}$, we may define U_{uc}^k as the k^{th} uniformly controlled R_z rotation with angle $\sqrt{\gamma}\mathbf{w}_k \cdot \mathbf{x}$, control the $|k \pmod{(d/2)}\rangle_{n-1}$ state and target the n^{th} qubit, this operation performs the following phase transformation to the n^{th} qubit when the control is the $|k \pmod{(d/2)}\rangle_{n-1}$ state, $U_{\text{uc}}^k(|k \pmod{(d/2)}\rangle_{n-1} \otimes 2^{-1/2}(|0\rangle + |1\rangle)) = |k \pmod{(d/2)}\rangle_{n-1} \otimes 2^{-1/2}(|0\rangle + e^{i\sqrt{\gamma}\mathbf{w}_k \cdot \mathbf{x}}|1\rangle)$, the desired QAFF mapping is obtained by applying the $d - 1$ uniformly controlled rotations $|\psi(\mathbf{x})\rangle = (\prod_{k=d/2}^{d-1} U_{\text{uc}}^k)(I^{\otimes n-1} \otimes X)(\prod_{k=1}^{d/2-1} U_{\text{uc}}^k)|+\rangle^{\otimes n}$; this method requires an X gate in the middle to change the phases of both the $|0\rangle$ and the $|1\rangle$ basis states of the n^{th} qubit; Fig 3b shows a particular 3-qubit circuit

example to prepare the QAFF. In Appendix A, we illustrate a proposal to prepare the QAFF with single R_z rotations and CNOTs gates, instead of uniformly controlled rotations, by performing the reparametrization $\{\sqrt{\gamma}\mathbf{w}_j \cdot \mathbf{x}\} \rightarrow \{\sqrt{\gamma}\boldsymbol{\theta}_j \cdot \mathbf{x}\}$, where the latter are the angles of the single-qubit R_z rotations; we also show that the depth of the algorithm, measured in the number of CNOTs, has order $O(d)$, which is independent of the size D of the original space.

Once $|\psi(\mathbf{x})\rangle$ and $|\psi(\mathbf{y})\rangle$ are prepared, we can compute $\hat{k}_{\{\mathbf{w}_j\}}(\mathbf{x}, \mathbf{y}) = |\langle \psi(\mathbf{x}) | \psi(\mathbf{y}) \rangle|^2$, by the quantum kernel estimation protocol [60], see Fig. 3a. Finally, to optimize the loss function, see Eq. 11, we initialize the components of the variational parameters $\{\mathbf{w}_j\}$ randomly from $U[0, 1]$, and use parameter-shift rule [61] to estimate the gradients.

The total complexity to train the QAFF in quantum computers is $O(TDd + Td^2R)$, where T is, as before, the number of data pairs $\{(\mathbf{x}_l, \mathbf{x}_m)\}_{1 \dots T}$ and R is the number of shots to estimate the gradients, see Appendix B. This quantum complexity does not improve the classical complexity of $O(TDd + Td^2)$, since the quantum algorithm requires R measurements of the kernel estimation circuit to get a good estimate of the gradients of the feature mapping. Considering that the classical QAFF has a lower complexity than the quantum QAFF and that the Q-DEMDE method requires an intermediate classical step to build the training density matrix, we choose to use classical QAFF to prepare the quantum mapping, however this quantum implementation may have applications in other quantum algorithms that do not require an intermediate classical preprocessing.

C. Q-DMKDE quantum circuit: estimating expectation values of density matrices

To implement the prediction phase of the Q-DEMDE, or the classical DMKDE in a quantum computer, see Eq. 5, we also propose a novel quantum protocol called Q-DMKDE to estimate the expected value of a mixed state

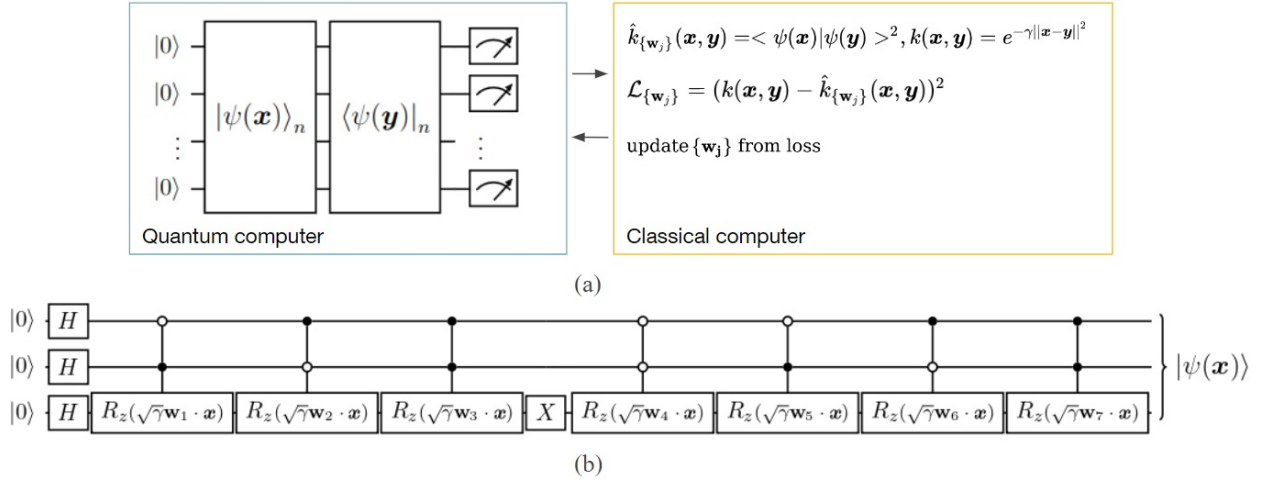


FIG. 3. Although the Q-DEMDE uses classical QAFF, we present an alternative variational algorithm to train the QAFF in quantum hardware. (a) Hybrid QAFF strategy with quantum kernel estimation protocol [60]. (b) Example of a quantum circuit to prepare the QAFF with 8 Fourier features and three qubits by means of multicontrolled R_z rotations, however, we may also prepare this state with single R_z rotations and CNOT gates as explained in Appendix A.

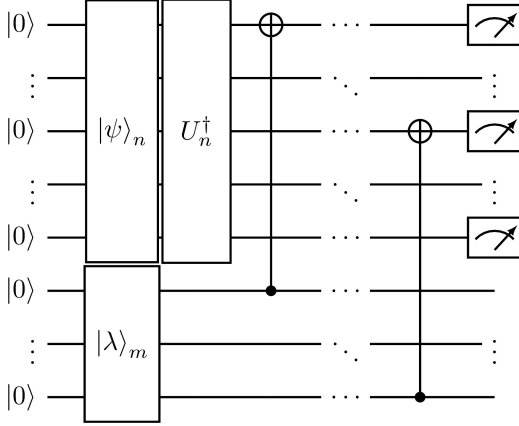


FIG. 4. Q-DMKDE quantum circuit to estimate the expected value of a density matrix from its spectral decomposition. The expected value of the density matrix is estimated by $P(|0\rangle_n) = \langle \psi | \rho | \psi \rangle = \langle \psi | V \Lambda V^\dagger | \psi \rangle$, where $|\psi\rangle$ and V are prepared in the first n qubits, and Λ in the last m qubits.

density matrix from its eigendecomposition in a qubit-based quantum computer, see Fig. 4. This circuit extends to qubits a previous method for estimating the expected value of a density operator in a high-dimensional quantum computer [19].

We want to compute the expected value of a density matrix $\rho \in \mathbb{C}^{d \times d}$ of rank $r \leq d$ with a quantum state $|\psi\rangle \in \mathbb{C}^d$ in a quantum computer. This calculation requires $n+m$ qubits, with $n = \lceil \log(d) \rceil$ and $m = \lceil \log(r) \rceil$. The first n qubits prepare the state $|\psi\rangle$ and the unitary matrix V^\dagger whose first r rows are the complex conjugate eigenvectors of ρ , and the remaining m qubits prepare the eigenvalues of the density matrix.

To begin with, as noted in [19], we have that,

$$\begin{aligned} \langle \psi | \rho | \psi \rangle &= \langle \psi | V \left(\sum_{i=0}^{r-1} \lambda_i |i\rangle \langle i| + \sum_{i=r}^{d-1} 0 |i\rangle \langle i| \right) V^\dagger | \psi \rangle \\ &= \sum_{i=0}^{r-1} \lambda_i |\langle i | V^\dagger | \psi \rangle|^2, \end{aligned} \quad (13)$$

where, $V \in \mathbb{C}^{d \times d}$ is a unitary matrix whose first r columns are the eigenvectors of ρ and $\Lambda = \sum_{i=0}^{r-1} \lambda_i |i\rangle \langle i|$ is the diagonal matrix of eigenvalues.

The proposed Q-DMKDE quantum circuit starts by initializing the first n qubits with the state $|\psi\rangle_n$, see the notation in Sect. III D, and the remaining m qubits with the state $|\lambda\rangle_m = \sum_{j=0}^{r-1} \sqrt{\lambda_j} |j\rangle_m$ that encodes the eigenvalues of ρ , see Fig. 4. This operation can be carried out thanks to amplitude encoding [58, 59]. We then have the complete state

$$|\psi\rangle_n \otimes |\lambda\rangle_m = |\psi\rangle_n \otimes \sum_{j=0}^{r-1} \sqrt{\lambda_j} |j\rangle_m. \quad (14)$$

Next, we build the unitary matrix U_n^\dagger in the first n qubits, see Eq. 15, whose first quadrant is composed of the unitary matrix V^\dagger and its fourth quadrant with an identity matrix I with rank $2^n - d$,

$$U_n^\dagger = \begin{pmatrix} V^\dagger & |0\rangle \\ \hline 0 & I \end{pmatrix}, \quad (15)$$

this unitary matrix U_n^\dagger is the conjugate transpose of U_n . Since the eigenvectors of ρ correspond to the first r columns of U , we can build U_n as an isometry from m to n qubits [57], see Sect. III E. We would have,

$$U_n^\dagger |\psi\rangle_n \otimes \sum_{j=0}^{r-1} \sqrt{\lambda_j} |j\rangle_m. \quad (16)$$

We can write the state of the first n qubits as, $U_n^\dagger |\psi\rangle_n = \sum_{i=0}^{d-1} a_i |i\rangle_n$. Where,

$$|a_i|^2 = |\langle i|_n U_n^\dagger |\psi\rangle_n|^2 = |\langle i| V^\dagger |\psi\rangle|^2, \quad (17)$$

namely, $|a_i|^2$ is the probability to measure $U_n^\dagger |\psi\rangle_n$ in the canonical state $|i\rangle_n$. Therefore, the circuit leads,

$$U_n^\dagger |\psi\rangle_n \otimes |\lambda\rangle_m = \sum_{i=0}^{d-1} a_i |i\rangle_n \otimes \sum_{j=0}^{r-1} \sqrt{\lambda_j} |j\rangle_m = \sum_{i=0}^{r-1} a_i \sqrt{\lambda_i} |i\rangle_n \otimes |i\rangle_m + \sum_{\{(i,j):i \neq j\}} a_i \sqrt{\lambda_j} |i\rangle_n \otimes |j\rangle_m. \quad (18)$$

Then, as shown in Fig. 4, we apply a cascade of m CNOT gates between the first and second halves of the circuit. The i^{th} CNOT operates with control the $(i+n)^{\text{th}}$ qubit and target the i^{th} qubit, with $i \in \{0, \dots, m-1\}$. The effect of this series of m CNOT gates can be observed by writing,

$$|i\rangle_n \otimes |j\rangle_m = \left| \sum_{k=0}^{n-1} b_k^i 2^k \right\rangle_n \otimes \left| \sum_{l=0}^{m-1} b_l^j 2^l \right\rangle_m, \quad (19)$$

where, $|b_0^i b_1^i \dots b_{n-1}^i\rangle$ and $|b_0^j b_1^j \dots b_{m-1}^j\rangle$ are the binary representations of $|i\rangle_n$ and $|j\rangle_m$ respectively. The m CNOT gates have the same depth as a single CNOT, as they can be parallelized in a quantum computer [62].

We represent this series of m CNOT gates with the $(n+m)$ -qubit unitary operation U_{n+m}^{CN} , where CN stands for CNOT. The outcome of this transformation is a qubit-wise summation modulo 2 (denoted by \oplus) on the first m qubits of the circuit,

$$U_{n+m}^{\text{CN}}(|i\rangle_n \otimes |j\rangle_m) = \left| \sum_{k=0}^{m-1} (b_k^i \oplus b_k^j) 2^k + \sum_{k=m}^{n-1} b_k^i 2^k \right\rangle_n \otimes \left| \sum_{l=0}^{m-1} b_l^j 2^l \right\rangle_m \\ = \left| \sum_{k=0}^{n-1} (b_k^i \oplus b_k^j) 2^k \right\rangle_n \otimes \left| \sum_{l=0}^{m-1} b_l^j 2^l \right\rangle_m$$

In the last line, we set $b_k^j = 0$ for $k \geq m$. If $i = j$, we have that,

$$U_{n+m}^{\text{CN}}(|i\rangle_n \otimes |i\rangle_m) = |0\rangle_n \otimes \left| \sum_{l=0}^{n-1} b_l^i 2^l \right\rangle_m$$

In contrast, if $i \neq j$, the state $\left| \sum_k (b_k^i \oplus b_k^j) 2^k \right\rangle_n$ would be distinct to the $|0\rangle_n$ state.

Therefore, after applying the series of m CNOT gates to the state of Eq. 18, the resulting state of the Q-DMKDE quantum circuit is

$$\sum_{i=0}^{r-1} a_i \sqrt{\lambda_i} |0\rangle_n \otimes |i\rangle_m \\ + \sum_{\{(i,j):i \neq j\}} a_i \sqrt{\lambda_j} \left| \sum_k (b_k^i \oplus b_k^j) 2^k \right\rangle_n \otimes |j\rangle_m.$$

By measuring the first n qubits the probability of state $|0\rangle_n$ would be,

$$P(|0\rangle_n) = \sum_{i=0}^{r-1} |a_i|^2 \lambda_i = \sum_{i=0}^{r-1} \lambda_i |\langle i| V^\dagger |\psi\rangle|^2 = \langle \psi | \rho | \psi \rangle,$$

see Eqs. 13 and 17.

Assuming we have access to the eigenvectors and eigenvalues of the density matrix, the total complexity of the Q-DMKDE quantum algorithm is $O(drS)$ since it takes $O(d)$ to prepare $|\psi\rangle_n$, $O(r)$ to prepare $|\lambda\rangle_m$, and $O(dr)$ to construct the isometry U_n , see Table I. In addition, we need to perform S measurements of the $|0\rangle_n$ bit string. Note that the classical algorithm has complexity $O(dr)$, therefore to achieve quantum advantage it is required to approximate the states $|\psi\rangle_n$, $|\lambda\rangle_m$ and the unitary matrix U_n , with quantum circuits of depth $O(\log d)$. Furthermore, the ansatz used in the Q-DMKDE quantum algorithm can be used to initialize a density matrix from its spectral decomposition starting from the $|0\rangle_n \otimes |0\rangle_m$ state, as illustrated in the SDM (spectral density matrix) ansatz in Appendix C.

D. Computational complexity analysis

In this section, we present the computational complexity of the proposed quantum-classical density estimation strategy Q-DEMDE using QRFF and QAFF, and we compare it with the complexities of the classical density estimation algorithms KDE [14, 15] and DMKDE [27]. For this purpose, we set T sample pairs to train classically the QAFF, N training data points which build the training density matrix (assuming $T > N$), and M test samples whose density we want to estimate, recalling that QRFF and QAFF map D -dimensional classical data points to a quantum feature space of dimension d , and r is the rank of the training density matrix. Furthermore, we set S , the number of quantum circuit measurements to perform the density estimation with Q-DMKDE algorithm. Table II summarizes the parameters of the density estimation methods.

Parameter	Description
N	No of training samples
M	No of testing samples
T	No of data pairs to train QAFF
D	Size of original data space
d	Size of the quantum feature space
r	No of eigenvalues of the density matrix
S	No of DE shots with Q-DMKDE
γ	Bandwidth of the Gaussian kernel

TABLE II. Summary of the parameters involved in the classical and quantum-classical density estimation algorithms KDE, DMKDE, Q-DEMDE.

Table III summarizes the computational complexity of the training and prediction phase from top to bottom of

the methods: kernel density estimation (KDE) [14, 15], DMKDE in classical hardware (C-DMKDE) [27], and the proposed quantum-classical DE method Q-DEMDE. For the C-DMKDE and Q-DEMDE we illustrate the complexity of the algorithms using both QRFF and QAFF and separate the complexity into training and testing stages, where the training phase consists of the construction of the training density matrix in classical or quantum hardware, see Eq. 4, and the test phase consists of the computation of the density estimation over test samples, see Eq. 5. We present the complexity analysis of each method separately and then the comparison between the methods.

1. Computational complexity of KDE

The computational complexity for simultaneously training and testing the KDE algorithm [14, 15] is $O(NMD)$, since it involves the estimation of the kernel between all the testing samples with all the training samples which leads to $O(NM)$ operations and each kernel calculation has complexity $O(D)$.

2. Computational complexity of C-DMKDE

The complexity of the C-DMKDE [27] with QAFF in the training phase is $O(Td \max(d, D))$, since it takes $O(T(Dd+d^2))$ to train the QAFF in a classical computer, see Appendix. B, and $O(Nd^2)$ to prepare the training density matrix, and the complexity of the testing phase is $O(Md \max(d, D))$, since it is required $O(MDd)$ to build the quantum features of the testing samples and $O(Md^2)$ to find the density estimates by computing the expectation value between each test quantum state and the training density matrix in a classical computer. The complexity analysis of the C-DMKDE with QRFF is similar to the case of QAFF, except that the training complexity changes from $O(Td \max(d, D))$ to $O(Nd \max(d, D))$, since it takes $O(NDd)$ to build the QRFF of the training samples.

3. Computational complexity and circuit depth of Q-DEMDE

The training complexity of the proposed quantum-classical density estimation model Q-DEMDE with QAFF is $O(Td \max(d, D) + d^2r)$, since it takes $O(TDd + Td^2)$ to train classically the quantum adaptive Fourier features, see Appendix. B, and $O(NDd)$ to estimate the QAFF map of the training data set, it also takes $O(Nd^2)$ to classically construct the training density matrix, and $O(d^2r)$ to classically compute its r eigenvalues and eigenvectors. The complexity of the prediction step of the Q-DEMDE with QAFF is $O(MDd + MdrS)$ which can be divided into $O(MDd)$ to build classically the QAFF of

the test samples and $O(MdrS)$ to estimate in a quantum computer their density values, because for each test sample, it takes $O(d)$ and $O(dr)$ to prepare the QAFF test state and the training density matrix respectively using the Q-DMKDE quantum density algorithm, see Sect. IV C, and it is required to measure the $|0\rangle_n$ bit string S times to obtain a good estimate of the density value. As in the C-DMKDE, the complexity of the Q-DEMDE with QRFF resembles the complexity of Q-DEMDE with QAFF, except that in the training phase its complexity changes to $O(Nd \max(d, D) + d^2r)$, since it is not required to optimize the quantum features.

To illustrate the circuit depth of the Q-DEMDE algorithm, we summarize in Table IV the approximate depth (number of CNOTS) and the qubit count of the quantum-classical subroutines QAFF, QRFF and Q-DMKDE. It is worth highlighting that the depth of the QRFF and QAFF does not depend on the size of the classical features D , but on the size of the Fourier representation d , which allows to represent high dimensional data in a quantum computer.

4. Computational complexity comparison

We summarize the complexity of the classical KDE, C-DMKDE and quantum-classical Q-DEMDE density estimation algorithms in Table III. This complexity analysis shows that the Q-DEMDE reduces the computational complexity of KDE in the regime where N is larger than d , and ND is larger than drS , nevertheless, it also illustrates no quantum advantage of using the Q-DEMDE over the classical DMKDE. Indeed, we observe that the proposed Q-DEMDE requires more resources compared to the classical algorithm since it needs to perform multiple measurements to find good estimates of the probability density values; this complexity drawback is shared by some other quantum machine learning algorithms of the state-of-art [20, 63, 64] that rely on estimating expectation values on quantum hardware, so solving this challenge represents an opportunity for the design of future quantum machine learning algorithms [65].

E. Alternative of the spectral decomposition: quantum-classical non-orthogonal density matrix density estimation (QNO-DEMDE)

We present an additional model called QNO-DEMDE, for quantum-classical density estimation with non-orthogonal density matrices. The method is an alternative of the Q-DEMDE method that does not require the spectral decomposition of the training density matrix, however, in Sect. IVE 2, we illustrate that the proposed Q-DEMDE is a more optimal method because the QNO-DEMDE has greater computational complexity. The steps of the QNO-DEMDE method are as follows: i) Use a classical computer to apply a feature map

DE Method	Quantum map	Train complexity	Test complexity
KDE [14, 15]	-	-	$O(NMD)$
C-DMKDE [27]	QRFF QAFF	$O(Nd \max(d, D))$ $O(Td \max(d, D))$	$O(Md \max(d, D))$
Q-DEMDE	QRFF QAFF	$O(Nd \max(d, D) + d^2 r)$ $O(Td \max(d, D) + d^2 r)$	$O(MDd + MdrS)$

TABLE III. Comparison of the computational complexity of the classical and quantum density estimation methods with QRFF and QAFF in training and prediction phases, with T sample pairs to train the QAFF, N training data points, M test samples, D the dimension of the classical data, d the dimension of the quantum feature map, r the number of eigenvalues of the training density matrix, and S the number of measurements in a quantum computer to find the density estimates with the Q-DMKDE algorithm.

Q-DEMDE Subroutine	Num. of qubits	Circuit depth
QRFF	$\log(d)$	d
QAFF	$\log(d)$	d
Q-DMKDE	$\log(dr)$	dr

TABLE IV. Number of qubits and approximate depth (number of CNOTS) of the Q-DEMDE quantum-classical subroutines: QAFF, QRFF and Q-DMKDE, in terms of the number of Fourier features d (same size of the training density matrix) and rank r of the eigendecomposition of the training density matrix. Here we assume d, r as powers of two

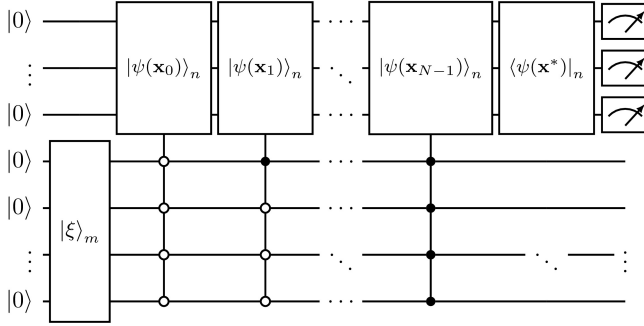


FIG. 5. QNO-DMKDE quantum circuit to estimate the expected value of a density matrix as an ensemble of pure states, here $|\xi\rangle_m = \sum_{i=0}^{N-1} \sqrt{1/N} |i\rangle_m$, $\{|\psi(\mathbf{x}_j)\rangle\}$ are the training features and $|\psi(\mathbf{x}^*)\rangle$ is the test feature whose density we aim to estimate.

to the training data samples $\{\mathbf{x}_j\} \rightarrow \{|\psi(\mathbf{x}_j)\rangle\}$ and the test sample $\mathbf{x}^* \rightarrow |\psi(\mathbf{x}^*)\rangle$ based on quantum random or quantum adaptive Fourier features, see Sect. IV A, ii) Use a quantum computer to prepare the training density matrix ρ_{train} , see Eq. 4, and to estimate the probability density of the test sample \mathbf{x}^* , see Eq. 5, by means of the QNO-DMKDE quantum circuit.

1. QNO-DMKDE quantum algorithm

The quantum non-orthogonal DMKDE (QNO-DMKDE) estimates the expected value of the training density matrix as a mixture of non-orthogonal pure states $\langle \psi(\mathbf{x}^*) | \rho_{\text{train}} | \psi(\mathbf{x}^*) \rangle$, where

$\rho_{\text{train}} = (1/N) \sum_{j=0}^{N-1} |\psi(\mathbf{x}_j)\rangle \langle \psi(\mathbf{x}_j)|$, and $\{|\psi(\mathbf{x}_j)\rangle\}$, $|\psi(\mathbf{x}^*)\rangle \in \mathbb{C}^d$ are the quantum features of the training data set and the test sample respectively. In contrast to the Q-DMKDE, this quantum algorithm does not require the spectral decomposition of ρ_{train} . The QNO-DMKDE algorithm requires $(m+n)$ qubits, such that $n = \lceil \log d \rceil$ and $m = \lceil \log N \rceil$. The method starts by building a purification of the training density matrix by initializing the pure state $|\xi\rangle_m = \sum_{i=0}^{N-1} \sqrt{1/N} |i\rangle_m$, on the last m qubits, followed by a series of N uniformly controlled isometries in the form of state preparations, with controls the last m qubits and targets the first n qubits; these controlled state preparations are applied following the structure of a multiplexer gate [58, 66]; the i^{th} controlled isometry sets the $|i\rangle_m$ state from the second half as the control and target the first n qubits, with the isometry U_n^i , that corresponds to a quantum state preparation $U_n^i |0\rangle_n \rightarrow |\psi(\mathbf{x}_i)\rangle_n$, as shown in Fig. 5. The resulting state of these N uniformly controlled isometries is the purification,

$$\sum_{i=0}^{N-1} \sqrt{\frac{1}{N}} |\psi(\mathbf{x}_i)\rangle_n \otimes |i\rangle_m. \quad (20)$$

We then apply an inverse state preparation \mathcal{U}_n^\dagger in the first n qubits, such that $\mathcal{U}_n |0\rangle_n = |\psi(\mathbf{x}^*)\rangle_n$, is an isometry that prepares the quantum test sample, thus obtaining,

$$(\mathcal{U}_n^\dagger \sum_{i=0}^{N-1} \sqrt{\frac{1}{N}} |\psi(\mathbf{x}_i)\rangle_n) \otimes |i\rangle_m, \quad (21)$$

and we conclude by performing a measurement over the first n qubits, obtaining that $P(|0\rangle_n) = (1/N) \sum_{i=0}^{N-1} |\langle \psi(\mathbf{x}^*) | \psi(\mathbf{x}_i) \rangle|^2 = \langle \psi(\mathbf{x}^*) | \rho_{\text{train}} | \psi(\mathbf{x}^*) \rangle$.

The computational complexity of the QNO-DMKDE quantum algorithm is $O(dNS)$ since it takes $O(dN)$ to construct the purification of the training density matrix, $O(d)$ to build the isometry which prepares the test quantum state and it is required S measurements of $|0\rangle_n$ basis state to estimate the probability density.

2. Computational complexity of the QNO-DEMDE

The computational complexity of both training and testing stages of the QNO-DEMDE with QAFF is $O(TD \max(d, D) + MDd + MNdS)$, assuming $T > N$, since it requires $O(TDd + Td^2)$ to train classically the QAFF, see Appendix. B, $O(NDd)$ and $O(MDd)$ to predict the Fourier features of the training and testing data respectively, and $O(MNdS)$ to find an estimation of the probability densities of the testing data, because for each test sample it is necessary to build the QNO-DMKDE quantum algorithm which has complexity $O(dNS)$, as explained in the previous section IV E 1. Furthermore, the complexity of QNO-DEMDE with QRFF is $O(NDd + MDd + MNdS)$, since it is not required to train the Fourier weights.

It should be noted that for most practical applications, it would be preferable to use the Q-DEMDE for quantum-classical density estimation, for instance, for both Q-DEMDE and QNO-DEMDE the computational complexity is dominated by the quantum density estimation protocols Q-DMKDE and QNO-DMKDE, which scale in the form $O(MdrS)$ and $O(MNdS)$, respectively. Indeed, in most cases, the number of training data N would be larger than the rank r of the training density matrix.

V. METHOD EVALUATION

In this section, we present the results of the proposed quantum-classical density estimation method Q-DEMDE for one and two-dimensional density estimation with both QRFF and QAFF in a quantum simulator and a real quantum computer.

A. One-dimensional quantum-classical density estimation

We present a demonstration of one-dimensional density estimation in both a quantum simulator and a real quantum computer.

1. Setup

As mentioned in Sect. III C, the DMKDE algorithm, along with quantum random or quantum adaptive Fourier features, encodes a probability distribution of the training data in a density matrix and estimates the probability density of new test samples by computing an expectation value.

To test the Q-DEMDE method with the quantum Fourier features, we constructed a one-dimensional probability density distribution corresponding to a mixture of two Gaussians. The training data set consisted of

1000 points sampled from the probability density function (pdf), whose probability density we wanted to estimate, and the test data set consisted of 250 equidistant points in $[-7, 7]$.

Two quantum feature maps, based on QAFF and QRFF, were applied to both the training and test data sets; we chose 4 Fourier components for each mapping. As in conventional RFF [28], the weights of the quantum random Fourier features were sampled from $\mathcal{N}(0, 1)$. To train in a classical computer the quantum adaptive Fourier features, we use the 1-dimensional Gaussian kernel training data set, see Sect. IV B 1, i.e., we used a set 1-dimensional data points sampled from $\mathcal{N}(0, 1)$ with $\gamma = 0.5$ as kernel training data samples, which allowed to better approximate the weights of the quantum Fourier features; when doing this feature learning the obtained weights also resulted with a standard deviation close to 1. We set $\gamma = 1$ when predicting the QRFF and QAFF mappings of the training and test data sets $\{\mathbf{x}_j\}$ and \mathbf{x}^* . We then constructed the training density matrix with dimensions 4×4 , see Eq. 4, and computed its spectral decomposition with 4 eigenvalues with a precision of 64 bytes on a classical computer.

For the prediction step, we computed the probability density estimator, see Eq. 5, which corresponds to the expected value of the training density matrix, with our proposed Q-DMKDE quantum circuit, see Fig. 4. We used the noisy QASM quantum simulator of the Qiskit IBM python library and the real IBM-Oslo quantum computer to estimate the expected value of the 4×4 training density matrix using 4 qubits and 12000 circuit measurements (shots); in Appendix E, we describe the characteristics of the IBM-Oslo quantum computer. Since we were working with a small number of features, we also performed a normalization of the density values by subtracting the minimum value from the density estimates; although this is not necessary for a large number of Fourier features. We evaluated the Q-DEMDE with QRFF and QAFF for density estimation, by comparing their density estimates with the real probability distribution that generated the data. For this purpose, we selected as metrics the Kullback-Leibler (KL) divergence, mean average error (MAE) and Spearman correlation which are widely used to compare probability distributions.

2. Results and discussion

We report three demonstrations of density estimation, see Fig. 6 and Table. V, two using the QASM quantum simulator for the Q-DMKDE and both QRFF and QAFF and one using QAFF and computing the density estimator on the real IBM-Oslo quantum computer.

In the subfigures of the left and center of Fig. 6, we show the probability density estimation with both quantum random and quantum adaptive Fourier features with the QASM simulator. In contrast to QRFF, the QAFF produces a better approximation of the pdf, especially in

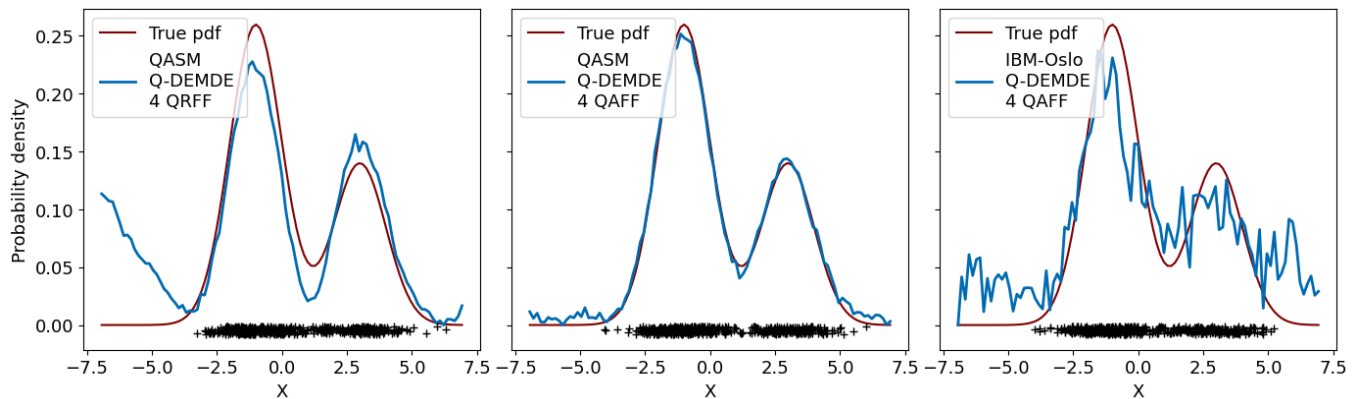


FIG. 6. Results of one-dimensional quantum-classical density estimation with 4 Fourier features: left, Q-DEMDE with QRFF in QASM simulator, center, Q-DEMDE with QAFF learned in a classical computer and predictions in the QASM quantum simulator, right, Q-DEMDE with QAFF learned in a classical computer and Q-DMKDE predictions in real IBM-Oslo quantum computer.

Method	Feature Map	KL-Div	MAE	Spearman
Q-DEMDE QASM	QRFF: 4	0.218	0.026	0.663
Q-DEMDE QASM	QAFF: 4	0.025	0.005	0.971
Q-DEMDE IBM QC	QAFF: 4	0.215	0.030	0.862

TABLE V. Results of one-dimensional quantum-classical density estimation using the Q-DEMDE method with four QRFF and four QAFF in the QASM quantum simulator and the real IBM-Oslo quantum computer. The best results are shown in bold.

low-density regions. Furthermore, the density estimation metrics shown in Table V illustrate that QAFF is more suitable for 1-dimensional density estimation in the case of a low number of Fourier features. In the subfigure of the right of Fig. 6, we present the results of QAFF learned in a classical computer and the density estimates predicted with the Q-DMKDE quantum algorithm in the real IBM-Oslo quantum computer. As expected, the results on the real quantum computer were much noisier than the results on the QASM simulator; however, the results and the density estimation metrics show that it is possible to perform 1-dimensional density estimation on real quantum computers with relatively good performance.

B. Two-dimensional quantum-classical density estimation

We evaluate the proposed hybrid density estimation method for two-dimensional density estimation.

1. Setup

We estimated the probability density functions of five two-dimensional data sets sampled from five two-dimensional distributions [67], named from top to bottom: Binomial, Potential 1, Potential 2, Arc and Star Eight, see Fig. 7; the statistical characteristics of these distributions are described in the Appendix F. We performed density estimation with three models: kernel density estimation (KDE) as a reference model, and the Q-DEMDE with both QRFF and QAFF with 32 components. The training data set for the density estimation tasks corresponded to 10000 points sampled from the two-dimensional distributions, while the test data set was constructed by dividing the five two-dimensional spaces by grids of 120×120 points.

We use a classical computer to build the QRFF and QAFF mappings. For each data set, we constructed the quantum random Fourier features by sampling the weights from $\mathcal{N}(\mathbf{0}, \mathbf{I}_2)$, and we used these random weights as the initial parameters to train the QAFF mapping. To illustrate the DE improvement of QAFF over QRFF, we trained the QAFF independently for each 2D data set, although we could have learned the quantum adaptive Fourier weights only once for all the 2D data sets, considering that we used the Gaussian kernel training data set for the kernel learning, see Sect. IV B 1, which is independent of the training and test density estimation data sets. After learning the optimal weights of the QAFF, for each of the five 2-dimensional data sets, we set the appropriate γ scaling parameter to predict the QRFF and QAFF; we also used the same corresponding γ parameter for the KDE method.

After establishing the QAFF and the QRFF maps for each 2-D data set, we built for each mapping the 32×32 training density matrix and found its spectral decomposition with 32 eigenvalues with a precision of 64 bytes in a classical computer. We then measured the expected

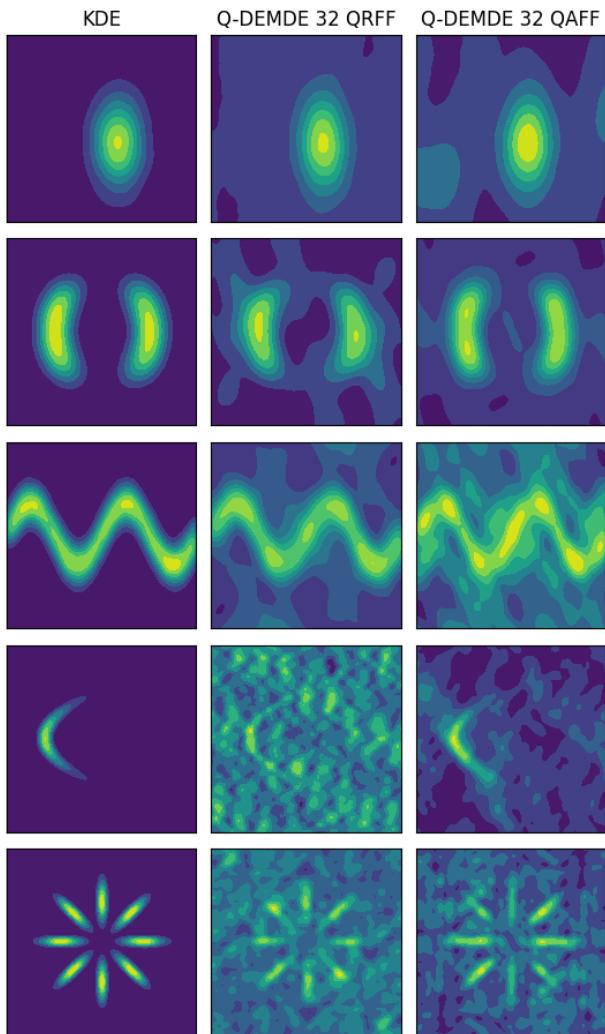


FIG. 7. Two-dimensional quantum-classical density estimation with a classical computer and a quantum simulator from PennyLane. From top to bottom, the two-dimensional data sets correspond to Binomial, Potential 1, Potential 2, Arc, and Star Eight.

value of the training density matrix with the quantum Fourier states of the test data set, using the 10-qubit Q-DMKDE quantum algorithm implemented in the PennyLane quantum library [68], obtaining the density estimation of the test data set. To validate the density estimation method, we compared the obtained probability distributions of Q-DEMDE with quantum random and quantum adaptive Fourier features with the probability density obtained with kernel density estimation, using KL-divergence, MAE and Spearman correlation.

2. Results and discussion

In Fig. 7, we show the density estimation of the test data set for all five 2-D data sets: in the left column,

we show the density estimation using kernel density estimation (KDE) [14, 15], in the middle figures, we plot the proposed quantum-classical DE method Q-DEMDE using 32 quantum random Fourier features, and in the right figures, we display the Q-DEMDE using 32 quantum adaptive Fourier features.

Since Q-DEMDE with QRFF and QAFF are both approximations of KDE, we aimed to replicate the 2-dimensional density estimation results of the KDE in all data sets. Despite the reduced number of quantum Fourier components, Fig. 7 and Table. VI show that both models with adaptive and random features obtained satisfactory results for two-dimensional quantum density estimation, albeit they could have been improved by increasing the number of Fourier components. Results also show that for most datasets there is an advantage of optimizing the Fourier weights with QAFF, illustrating that this adaptive mapping improves the kernel approximation. Out of the five data sets, the Arc and Star Eight were the most challenging data sets for density estimation considering that they required to approximate a kernel with a small bandwidth parameter.

It is worth mentioning that the proposed hybrid density estimation method is non-parametric, i.e., it does not require a prior probability distribution to fit the data, in contrast to parametric density estimation [12, 13], and it is optimization-free. Furthermore, although we did not perform two-dimensional density estimation in real quantum hardware, the quantum simulation used a low number of qubits (only 10), showing that Q-DEMDE might be suitable for current quantum hardware.

Data Set	Metric	Q-DEMDE 32 QRFF	Q-DEMDE 32 QAFF
Binomial	KL-Div	0.784	0.824
	MAE	0.025	0.024
	Spearman	0.750	0.425
Potential 1	KL-Div	0.571	0.555
	MAE	0.045	0.043
	Spearman	0.704	0.782
Potential 2	KL-Div	0.789	0.946
	MAE	0.171	0.164
	Spearman	0.726	0.806
Arc	KL-Div	2.713	2.193
	MAE	0.159	0.020
	Spearman	0.050	0.219
Star Eight	KL-Div	1.643	1.626
	MAE	0.157	0.159
	Spearman	0.230	0.353

TABLE VI. 2D quantum-classical density estimation results using the Q-DEMDE algorithm with both QRFF and QAFF. These results illustrate the similarity between the probability densities of test data obtained with the quantum-classical Q-DEMDE method and the classical KDE algorithm. The best results are shown in bold.

3. Additional: Results of hybrid density estimation with quantum variational QAFF

While the proposed Q-DEMDE strategy uses classical computers to optimize the quantum adaptive Fourier features, in Sect. IV B 2, we describe an alternative method to train the QAFF in quantum hardware using a quantum variational algorithm. In Appendix D, we include some additional quantum simulations that show that it is possible to perform 2-dimensional density estimation with the Q-DEMDE method using the QAFF optimized in a PennyLane noiseless quantum simulator. Although the Q-DEMDE method with classical QAFF has less computational complexity and it is therefore more optimal for hybrid density estimation, the feasibility of learning the QAFF mapping in quantum hardware may have applications to other hybrid quantum machine learning methods that, unlike the Q-DEMDE algorithm, do not require an intermediate classical computation.

VI. METHOD APPLICATION: QUANTUM-CLASSICAL ANOMALY DETECTION

In this section, we present a quantum-classical anomaly detection strategy as an application of our proposed hybrid density estimation method, see Fig. 8.

Anomaly detection aims to determine which samples from a given data set are “ordinary” or “normal” (being the interpretation of “normal” defined for each particular case) and which samples depart, or are deviated, from “normal” data (commonly known as “anomalies”). Some common applications of anomaly detection methods include fraud detection [10] and medical diagnosis [69]. This problem has been widely addressed in classical computers [70, 71], while quantum anomaly detection is a more recent field, from which some proposals have shown notable speed-ups in contrast to their classical counterparts [17, 72, 73].

In order to detect anomalous data in a given data set, the proposed method starts by dividing the data samples into three partitions: train, validation, and test, maintaining the same proportion of “normal” and “anomalous” data in all three partitions. After this, the method performs the following steps: i) use the proposed quantum-classical density estimation method Q-DEMDE to estimate the probability density values of all samples in validation and test partitions with the training partition, ii) use the validation data set to select a percentile-based threshold to separate the samples: if a sample has a density lower than the threshold, then it is considered an “anomalous” sample, and iii) finally, use this threshold to classify “normal” and “anomalous” data in the test partition. The main assumption on which we base this approach is that, unlike “normal” samples, the “anomalous” samples lie in regions with lower probability density values, as shown in Fig. 8.

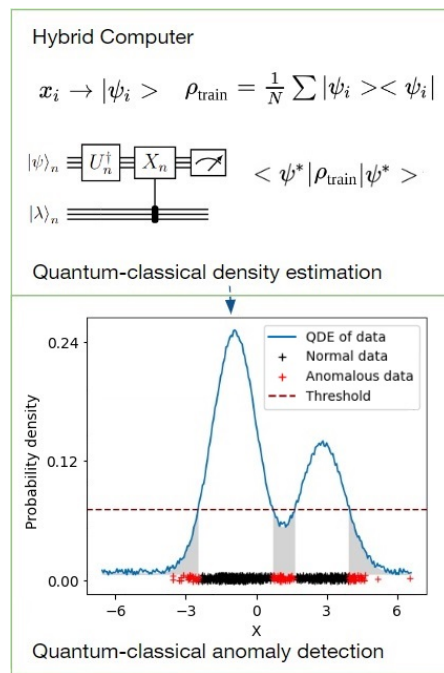


FIG. 8. Quantum-classical anomaly detection model for quantum computers based on the proposed quantum-classical density estimation strategy Q-DEMDE. Use Q-DEMDE to find the density values of the test data, and set a threshold to classify anomalous data, assuming that anomalous samples are found in low-density regions

A. QAD: Setup

We used the quantum-classical density estimation method Q-DEMDE to detect anomalies in a previously labeled AD data set. We used a modified version, from Ref. [74], of the Cardiocography data set from the UCI Machine Learning Repository related to fetal heart rate. It consists of 1831 samples, where each sample contains 21 attributes, with two classes: the *normal* class for the inliers, and the *pathologic* class for the outliers. This data set was divided into three partitions: training (60%), validation (20%), and test (20%), all of which contained both normal samples and outliers in the same proportion (approximately 9.6% of all samples were labeled as outliers).

As a first step, QRFF and QAFF were applied to the samples of all partitions as quantum feature mappings. We worked with 4 and 8 Fourier features corresponding to quantum states of 2 and 3 qubits respectively. The QAFF were trained using a classical computer. To train the QAFF with $\gamma = 0.5$, we used the Gaussian kernel training data set, see Sect. IV B 1, corresponding to 1×10^5 samples from $\mathcal{N}(\mathbf{0}, \frac{1}{21} \mathbf{I}_{21})$, the number of trainable parameters, which corresponds to the Fourier weights, were respectively $21 \times 4 = 84$ and $21 \times 8 = 168$ in the cases of 4 and 8 components. Once we learned the Fourier weights, we predicted the quantum Fourier features of the training, test and validation data sets by searching for the

optimal value of γ of the kernel (considering only powers of two ranging from 2^{-10} to 2^0), then setting a value of $\gamma = 2^{-7}$ for both QRFF and QAFF. We also used a classical computer to build the 4×4 and 8×8 training density matrices, see Eq. 4, and to compute their spectral decompositions. We then performed the density estimations with the 4-qubit and 6-qubit Q-DMKDE quantum algorithm in a noiseless quantum simulator of the PennyLane quantum library [68]. As it is common in anomaly detection tasks, the labels were not used to train the algorithm.

After performing the density estimations of the validation and test partitions, we classified each sample as “normal” or “outlier” by comparing its density value with a threshold value t . We used the validation partition to search for the threshold by setting a percentile value p such that 9.6% of the samples had a density below t and were thus considered anomalous samples. We then used the obtained boundary t to classify the testing data.

We also performed a demonstration of the QAD algorithm on the real IBM-Oslo quantum computer, refer to Appendix E for its characteristics. To achieve this, we first applied the QRFF and QAFF mappings to all three data partitions using a classical computer with 4 Fourier features and $\gamma = 2^{-5}$. Due to satisfactory results, we directly used the anomaly detection data to train the QAFF, as described in Sect. IV B 1, instead of the Gaussian synthetic kernel training data, although for a larger number of Fourier features and more complex data sets the synthetic Gaussian data set would be the preferable choice. Once the Fourier mappings were constructed, we used 4 qubits to prepare the training density matrix from its spectral decomposition using the Q-DMKDE quantum algorithm in the IBM-Oslo quantum processor, and estimated the probability densities of the test and validation data sets using 12000 shots.

We report the F1 score of the “anomalous” class, the accuracy, and the AUC (area under the characteristic curve). Since the random weights of the QRFF and the random initialization of the QAFF produce slightly different DE results in the case of a small number of Fourier features, we performed ten trials with different random seeds using the PennyLane quantum simulator. In contrast, in the real IBM-Oslo quantum computer, we performed the quantum demonstration only once for both quantum mappings. Furthermore, we initialized the weights of the QAFF from a uniform distribution $U[0, 1]$ in all cases, considering that the results were not strongly affected by the initial distribution of the Fourier weights.

B. QAD: Results and discussion

The results obtained by applying the proposed methods for hybrid anomaly detection with the PennyLane quantum simulator are reported in Tables VII and VIII. Compared to QRFF, the QAFF obtained better results in the three evaluated metrics, F1 Score, accuracy, and

AUC, thanks to the optimization of the Fourier weights. Regarding the standard deviations, we observe more consistent results across different trials with QAFF, which shows that QRFF is more sensitive to randomness than QAFF in a low-dimensional setting.

Method	F1 Score	Accuracy	AUC
Q-DEMDE 4 QRFF	0.422 ± 0.073	0.896 ± 0.013	0.776 ± 0.061
Q-DEMDE 4 QAFF	0.455 ± 0.067	0.899 ± 0.010	0.852 ± 0.051

TABLE VII. Obtained metrics for 10 hybrid anomaly detection trials on Cardio data set using Q-DEMDE method with 4 Fourier features for both QRFF and QAFF with the PennyLane quantum simulator.

Method	F1 Score	Accuracy	AUC
Q-DEMDE 8 QRFF	0.516 ± 0.126	0.911 ± 0.020	0.920 ± 0.039
Q-DEMDE 8 QAFF	0.573 ± 0.083	0.920 ± 0.010	0.915 ± 0.028

TABLE VIII. Obtained metrics for 10 hybrid anomaly detection trials on Cardio data set using Q-DEMDE method with 8 Fourier features for both QRFF and QAFF with the PennyLane quantum simulator.

Furthermore, in Table IX, we present the results of the hybrid anomaly detection algorithm on the real IBM-Oslo quantum computer; we performed only one demonstration of the QAD strategy for each quantum mapping. The results follow a similar pattern as in the quantum simulator: QAFF leads to higher performance than QRFF. In contrast to the quantum simulator, the demonstration with QRFF on the real quantum computer presented inferior results, probably because the density predictions with random features had low variance, making it difficult to make a distinction between the two classes due to quantum noise. Nevertheless, the Q-DEMDE with QAFF in the real quantum computer obtained satisfactory results for the anomaly detection task, showing that this strategy is suitable for current quantum devices.

Method	F1 Score	Accuracy	AUC
Q-DEMDE 4 QRFF IBM-Oslo	0.170	0.867	0.541
Q-DEMDE 4 QAFF IBM-Oslo	0.648	0.932	0.933

TABLE IX. Obtained metrics for hybrid anomaly detection on the real IBM-Oslo quantum computer using the Q-DEMDE density estimation strategy with both QRFF and QAFF with 4 Fourier components. We used a classical computer to learn the optimal QAFF, and the real quantum computer to predict the density of validation and test samples with the Q-DMKDE quantum circuit.

VII. CONCLUSIONS

In this article, we presented a quantum-classical density estimation method called Q-DEMDE for current quantum computers based on the expected values of density matrices and quantum Fourier features. Within our method, we proposed a quantum protocol for mixed-state preparation and expected value estimation, which was used as a subroutine to implement the classical density estimation algorithm DMKDE [27] in quantum hardware. We also introduced two quantum feature maps called quantum random and quantum adaptive Fourier features, which allow to approximate a Gaussian kernel between data samples in both classical and quantum computers. We performed various demonstrations on different data sets for density estimation on a quantum simulator and on a real quantum computer.

The quantum-classical density estimation results show that it is possible to exploit the properties of mixed states and Fourier features to efficiently represent probability distributions of data in quantum hardware. A key feature of the proposed hybrid DE method is that it is non-parametric, i.e., it does not assume a prior probability distribution to fit the training data, in contrast to parametric quantum DE methods [17, 18]. Furthermore, the Q-DEMDE method with the QRFF map is optimization-free, i.e., it does not require any optimization, while the Q-DEMDE method with QAFF requires optimization only to construct the quantum map. Although the Q-DEMDE algorithm does not achieve a quantum advantage over the classical DMKDE, it shows that it is possible to perform quantum-classical density estimation with a reduced number of quantum Fourier features and relatively small quantum circuits, illustrating its viability for present-day quantum computers.

We also presented an application of the hybrid density

estimation method for quantum-classical anomaly detection. Despite the current limitations of quantum hardware, the Q-DEMDE strategy showed satisfactory results for anomaly detection in a real quantum computer. Considering the numerous other applications of density estimation [1–3, 5, 6], the results indicate that the proposed hybrid density estimation method can be used as a building block for other quantum machine learning algorithms, and could provide novel avenues to solve new problems with quantum computers.

Future work of the proposed quantum-classical density estimation technique includes comparing our method with other classical and quantum density estimation methods, exploring other quantum density estimation algorithms that could possibly achieve quantum advantage, and integrating the proposed Q-DMKDE quantum circuit with variational quantum algorithms to learn mixed quantum states in quantum hardware.

CODE AVAILABILITY

The source code necessary to replicate the demonstrations presented in this paper is available in the following GitHub repository <https://github.com/diegour1/QDEMDE>.

ACKNOWLEDGMENTS

We acknowledge the use of IBM Quantum services for this work. The views expressed in this work are those of the authors and do not reflect the official policy or position of IBM or the IBM Quantum team. D.H.U. acknowledges Google Research for the support through the Google Ph.D. Fellowship.

-
- [1] S. A. Bigdeli, G. Lin, L. A. Dunbar, T. Portenier, and M. Zwicker, Learning generative models using denoising density estimators, *IEEE Transactions on Neural Networks and Learning Systems* (2023).
 - [2] B. Nachman and D. Shih, Anomaly detection with density estimation, *Phys. Rev. D* **101**, 075042 (2020).
 - [3] W. Hu, J. Gao, B. Li, O. Wu, J. Du, and S. Maybank, Anomaly detection using local kernel density estimation and context-based regression, *IEEE Transactions on Knowledge and Data Engineering* **32**, 218 (2018).
 - [4] F. D. Bortoloti, E. de Oliveira, and P. M. Ciarelli, Supervised kernel density estimation k-means, *Expert Systems with Applications* **168**, 114350 (2021).
 - [5] C. Fraley and A. E. Raftery, Model-based clustering, discriminant analysis, and density estimation, *Journal of the American statistical Association* **97**, 611 (2002).
 - [6] T. K. Anderson, Kernel density estimation and k-means clustering to profile road accident hotspots, *Accident Analysis & Prevention* **41**, 359 (2009).
 - [7] N. R. Gudhe, H. Behravan, M. Sudah, H. Okuma, R. Vanninen, V.-M. Kosma, and A. Mannermaa, Area-based breast percentage density estimation in mammograms using weight-adaptive multitask learning, *Scientific reports* **12**, 12060 (2022).
 - [8] H. Kato, Development of a spatio-temporal analysis method to support the prevention of covid-19 infection: space-time kernel density estimation using gps location history data, *Urban Informatics and Future Cities* , 51 (2021).
 - [9] L. Srikanth and I. Srikanth, A case study on kernel density estimation and hotspot analysis methods in traffic safety management, in *2020 International Conference on COMMunication Systems & NETWORKS (COMSNETS)* (IEEE, 2020) pp. 99–104.
 - [10] V. Van Vlasselaer, C. Bravo, O. Caelen, T. Eliassi-Rad, L. Akoglu, M. Snoeck, and B. Baesens, APATE: A novel approach for automated credit card transaction fraud detection using network-based extensions, *Decision Support Systems* **75**, 38 (2015).

- [11] G. Papamakarios, T. Pavlakou, and I. Murray, Masked autoregressive flow for density estimation, in *Advances in Neural Information Processing Systems*, Vol. 30, edited by I. Guyon, U. V. Luxburg, S. Bengio, H. Wallach, R. Fergus, S. Vishwanathan, and R. Garnett (Curran Associates, Inc., 2017).
- [12] M. K. Varanasi and B. Aazhang, Parametric generalized gaussian density estimation, *The Journal of the Acoustical Society of America* **86**, 1404 (1989).
- [13] V. Vapnik and S. Mukherjee, Support vector method for multivariate density estimation, in *Advances in Neural Information Processing Systems*, Vol. 12, edited by S. Solla, T. Leen, and K. Müller (MIT Press, 1999).
- [14] M. Rosenblatt, Remarks on Some Nonparametric Estimates of a Density Function, <https://doi.org/10.1214/aoms/1177728190> **27**, 832 (1956).
- [15] E. Parzen, On Estimation of a Probability Density Function and Mode, *The Annals of Mathematical Statistics* **33**, 1065 (1962).
- [16] Z. Wang and D. W. Scott, Nonparametric density estimation for high-dimensional data—algorithms and applications, *Wiley Interdisciplinary Reviews: Computational Statistics* **11**, e1461 (2019).
- [17] J.-M. Liang, S.-Q. Shen, M. Li, and L. Li, Quantum anomaly detection with density estimation and multivariate gaussian distribution, *Physical Review A* **99**, 052310 (2019).
- [18] M. Guo, H. Liu, Y. Li, W. Li, F. Gao, S. Qin, and Q. Wen, Quantum algorithms for anomaly detection using amplitude estimation, *Physica A: Statistical Mechanics and its Applications* **604**, 127936 (2022).
- [19] D. H. Useche, A. Giraldo-Carvajal, H. M. Zuluaga-Bucheli, J. A. Jaramillo-Villegas, and F. A. González, Quantum measurement classification with qudits, *Quantum Information Processing* 2021 21:1 **21**, 1 (2021).
- [20] V. Vargas-Calderón, F. A. González, and H. Vinck-Posada, Optimisation-free density estimation and classification with quantum circuits, *Quantum Machine Intelligence* **4**, 1 (2022).
- [21] S. Lloyd, M. Mohseni, and P. Rebentrost, Quantum principal component analysis, *Nature Physics* **10**, 631 (2014).
- [22] P. W. Shor, Algorithms for quantum computation: Discrete logarithms and factoring, *Proceedings - Annual IEEE Symposium on Foundations of Computer Science, FOCS*, 124 (1994).
- [23] S. Haroche, Entanglement, decoherence and the quantum/classical boundary, *Physics today* **51**, 36 (1998).
- [24] J. Preskill, Quantum computing in the nisq era and beyond, *Quantum* **2**, 79 (2018).
- [25] H. Lee, K. Jun, B. C. Kim, M. M. Woo, P. Rao, P. Castillo, and K. Yu, Quantum convolutional neural networks on NISQ processors, in *Quantum Communications and Quantum Imaging XIX*, Vol. 11835, edited by K. S. Deacon and R. E. Meyers, International Society for Optics and Photonics (SPIE, Bellingham, Washington, 2021) p. 1183509.
- [26] L. Bianchi, Robust quantum classifiers via nisq adversarial learning, *Nature Computational Science* **2**, 699 (2022).
- [27] F. A. González, A. Gallego, S. Toledo-Cortés, and V. Vargas-Calderón, Learning with density matrices and random features, *Quantum Machine Intelligence* **4**, 1 (2022).
- [28] A. Rahimi and B. Recht, Random features for large-scale kernel machines, in *Advances in Neural Information Processing Systems 20 - Proceedings of the 2007 Conference* (2009).
- [29] C. Blank, A. J. da Silva, L. P. de Albuquerque, F. Petrucione, and D. K. Park, Compact quantum distance-based binary classifier, arXiv preprint arXiv:2202.02151 (2022).
- [30] N. A. Nghiem, S. Y.-C. Chen, and T.-C. Wei, Unified framework for quantum classification, *Phys. Rev. Res.* **3**, 033056 (2021).
- [31] D. F. V. James, P. G. Kwiat, W. J. Munro, and A. G. White, Measurement of qubits, *Phys. Rev. A* **64**, 052312 (2001).
- [32] Y. Li, K. Zhang, J. Wang, and S. Kumar, Learning adaptive random features, *Proceedings of the AAAI Conference on Artificial Intelligence* **33**, 4229 (2019).
- [33] F. A. González, R. Ramos-Pollán, and J. A. Gallego-Mejia, Kernel density matrices for probabilistic deep learning (2023), arXiv:2305.18204 [cs.LG].
- [34] P. Rebentrost, M. Mohseni, and S. Lloyd, Quantum support vector machine for big data classification, *Physical review letters* **113**, 130503 (2014).
- [35] C. Blank, D. K. Park, J.-K. K. Rhee, and F. Petrucione, Quantum classifier with tailored quantum kernel, *npj Quantum Information* **6**, 1 (2020).
- [36] G. Sergioli, R. Giuntini, and H. Freytes, A new quantum approach to binary classification, *PloS one* **14**, e0216224 (2019).
- [37] C. H. Bennett, G. Brassard, S. Popescu, B. Schumacher, J. A. Smolin, and W. K. Wootters, Purification of noisy entanglement and faithful teleportation via noisy channels, *Physical review letters* **76**, 722 (1996).
- [38] A. Peruzzo, J. McClean, P. Shadbolt, M.-H. Yung, X.-Q. Zhou, P. J. Love, A. Aspuru-Guzik, and J. L. O’Brien, A variational eigenvalue solver on a photonic quantum processor, *Nature communications* **5**, 1 (2014).
- [39] M. A. Nielsen and I. L. Chuang, *Quantum Computation and Quantum Information: 10th Anniversary Edition*, *Quantum Computation and Quantum Information* 10.1017/CBO9780511976667 (2010).
- [40] M. Cramer, M. B. Plenio, S. T. Flammia, R. Somma, D. Gross, S. D. Bartlett, O. Landon-Cardinal, D. Poulin, and Y. K. Liu, Efficient quantum state tomography, *Nature Communications* 2010 1:1 **1**, 1 (2010).
- [41] F. A. González, V. Vargas-Calderón, and H. Vinck-Posada, Classification with quantum measurements, *Journal of the Physical Society of Japan* **90**, 044002 (2021), <https://doi.org/10.7566/JPSJ.90.044002>.
- [42] A. Kammonen, J. Kiessling, P. Plecháč, M. Sandberg, and A. Szepessy, Adaptive random fourier features with metropolis sampling, *Foundations of Data Science* **2**, 309 (2020).
- [43] Y. Liu, Y. Xu, J. Yang, and S. Jiang, A Polarized Random Fourier Feature Kernel Least-Mean-Square Algorithm, *IEEE Access* **7**, 50833 (2019).
- [44] R. Agrawal, T. Campbell, J. Huggins, and T. Broderick, Data-dependent compression of random features for large-scale kernel approximation, in *Proceedings of the Twenty-Second International Conference on Artificial Intelligence and Statistics*, *Proceedings of Machine Learning Research*, Vol. 89, edited by K. Chaudhuri and M. Sugiyama (PMLR, 2019) pp. 1822–1831.

- [45] H. Yamasaki, S. Subramanian, S. Sonoda, and M. Koashi, Learning with optimized random features: Exponential speedup by quantum machine learning without sparsity and low-rank assumptions, *Advances in neural information processing systems* **33**, 13674 (2020).
- [46] J. Xie, F. Liu, K. Wang, and X. Huang, Deep kernel learning via random fourier features, *arXiv preprint arXiv:1910.02660* (2019).
- [47] E. G. Băzăvan, F. Li, and C. Sminchisescu, Fourier Kernel Learning, *Lecture Notes in Computer Science (including subseries Lecture Notes in Artificial Intelligence and Lecture Notes in Bioinformatics)* **7573 LNCS**, 459 (2012).
- [48] M. Schuld, R. Sweke, and J. J. Meyer, Effect of data encoding on the expressive power of variational quantum-machine-learning models, *Physical Review A* **103**, 032430 (2021).
- [49] V. Havlíček, A. D. Córcoles, K. Temme, A. W. Harrow, A. Kandala, J. M. Chow, and J. M. Gambetta, Supervised learning with quantum-enhanced feature spaces, *Nature* **567**, 209 (2019).
- [50] R. Chatterjee and T. Yu, Generalized coherent states, reproducing kernels, and quantum support vector machines, *arXiv preprint arXiv:1612.03713* (2016).
- [51] M. Schuld, F. Petruccione, M. Schuld, and F. Petruccione, Quantum models as kernel methods, *Machine Learning with Quantum Computers*, 217 (2021).
- [52] E. Stoudenmire and D. J. Schwab, Supervised learning with tensor networks, *Advances in neural information processing systems* **29** (2016).
- [53] W. Rudin, *Fourier analysis on groups* (Courier Dover Publications, Mineola, New York, 2017).
- [54] V. C. Raykar, R. Duraiswami, and L. H. Zhao, Fast computation of kernel estimators, *Journal of Computational and Graphical Statistics* **19**, 205 (2010).
- [55] C. Yang, R. Duraiswami, and L. S. Davis, Efficient kernel machines using the improved fast gauss transform, *Advances in neural information processing systems* **17** (2004).
- [56] Yang, Duraiswami, and Gumerov, Improved fast gauss transform and efficient kernel density estimation, in *Proceedings ninth IEEE international conference on computer vision* (IEEE, 2003) pp. 664–671.
- [57] R. Iten, R. Colbeck, I. Kukuljan, J. Home, and M. Christandl, Quantum circuits for isometries, *Phys. Rev. A* **93**, 032318 (2016).
- [58] V. V. Shende, S. S. Bullock, and I. L. Markov, Synthesis of quantum-logic circuits, *IEEE Transactions on Computer-Aided Design of Integrated Circuits and Systems* **25**, 1000 (2006).
- [59] M. Möttönen, J. J. Vartiainen, V. Bergholm, and M. M. Salomaa, Transformation of quantum states using uniformly controlled rotations, *Quantum Information & Computation* **5**, 467 (2005).
- [60] Y. Liu, S. Arunachalam, and K. Temme, A rigorous and robust quantum speed-up in supervised machine learning, *Nature Physics* **17**, 1013 (2021).
- [61] K. Mitarai, M. Negoro, M. Kitagawa, and K. Fujii, Quantum circuit learning, *Physical Review A* **98**, 032309 (2018).
- [62] L. Cincio, Y. Subaşı, A. T. Sornborger, and P. J. Coles, Learning the quantum algorithm for state overlap, *New Journal of Physics* **20**, 113022 (2018).
- [63] M. Schuld, A. Bocharov, K. M. Svore, and N. Wiebe, Circuit-centric quantum classifiers, *Physical Review A* **101**, 032308 (2020).
- [64] W. M. Watkins, S. Y.-C. Chen, and S. Yoo, Quantum machine learning with differential privacy, *Scientific Reports* **13**, 2453 (2023).
- [65] F. R. Cardoso, D. Y. Akamatsu, V. L. Campo Junior, E. I. Duzzioni, A. Jaramillo, and C. J. Villas-Boas, Detailed account of complexity for implementation of circuit-based quantum algorithms, *Frontiers in Physics*, 582 (2021).
- [66] M. Möttönen, J. J. Vartiainen, V. Bergholm, and M. M. Salomaa, Quantum circuits for general multiqubit gates, *Physical review letters* **93**, 130502 (2004).
- [67] J. A. Gallego-Mejia and F. A. González, Demande: Density matrix neural density estimation, *IEEE Access* **11**, 53062 (2023).
- [68] V. Bergholm, J. Izaac, M. Schuld, C. Gogolin, M. S. Alam, S. Ahmed, J. M. Arrazola, C. Blank, A. Delgado, S. Jahangiri, *et al.*, PennyLane: Automatic differentiation of hybrid quantum-classical computations, *arXiv preprint arXiv:1811.04968* (2018).
- [69] L. F. Chen, An improved negative selection approach for anomaly detection: with applications in medical diagnosis and quality inspection, *Neural Computing and Applications* 2011 22:5 **22**, 901 (2011).
- [70] C. C. Noble and D. J. Cook, Graph-based anomaly detection, in *Proceedings of the Ninth ACM SIGKDD International Conference on Knowledge Discovery and Data Mining*, KDD '03 (Association for Computing Machinery, New York, NY, USA, 2003) p. 631–636.
- [71] F. A. González and D. Dasgupta, Anomaly detection using real-valued negative selection, *Genetic Programming and Evolvable Machines* **4**, 383 (2003).
- [72] N. Liu and P. Rebentrost, Quantum machine learning for quantum anomaly detection, *Physical Review A* **97**, 042315 (2018).
- [73] D. Herr, B. Obert, and M. Rosenkranz, Anomaly detection with variational quantum generative adversarial networks, *Quantum Science and Technology* **6**, 045004 (2021).
- [74] C. C. Aggarwal and S. Sathe, Theoretical Foundations and Algorithms for Outlier Ensembles, *ACM SIGKDD Explorations Newsletter* **17**, 24 (2015).
- [75] O. Perdomo, V. Leyton-Ortega, and A. Perdomo-Ortiz, Entanglement types for two-qubit states with real amplitudes, *Quantum Information Processing* **20**, 1 (2021).
- [76] N. Ezzell, E. M. Ball, A. U. Siddiqui, M. M. Wilde, A. T. Sornborger, P. J. Coles, and Z. Holmes, Quantum mixed state compiling, *arXiv preprint arXiv:2209.00528* (2022).
- [77] G. Di Bartolomeo, M. Vischi, F. Cesa, R. Wixinger, M. Grossi, S. Donadi, and A. Bassi, Noisy gates for simulating quantum computers, *Physical Review Research* **5**, 043210 (2023).

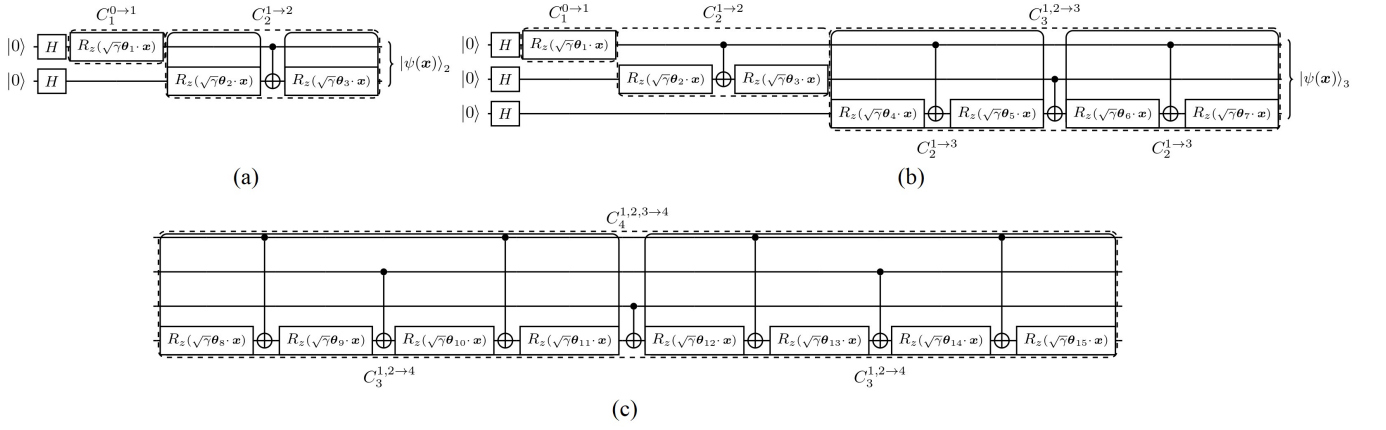


FIG. 9. Proposed quantum circuits for the Quantum adaptive Fourier features operation, (a) shows the circuit for two qubits and a size of 4 QAFF, and (b) shows the circuit for three qubits and 8 QAFF. As an example of the recursive construction of these operations, (c) illustrates the operation $C_4^{1,2,3 \rightarrow 4}$ of the circuit for 16 QAFF, formed by two copies of the block $C_3^{1,2 \rightarrow 3}$ in (b) and a CNOT gate.

Appendix A: Quantum adaptive Fourier features in a quantum computer with one and two qubit gates

We present the quantum circuit implementation of the quantum adaptive Fourier features mapping,

$$|\psi(\mathbf{x})\rangle_n = \sqrt{\frac{1}{d}} [1, e^{i\sqrt{\gamma}\mathbf{w}_1 \cdot \mathbf{x}}, e^{i\sqrt{\gamma}\mathbf{w}_2 \cdot \mathbf{x}}, \dots, e^{i\sqrt{\gamma}\mathbf{w}_{d-1} \cdot \mathbf{x}}]', \quad (\text{A1})$$

with the use of single qubit gates and CNOT gates, instead of uniformly controlled rotations, see Sect. IV B 2. The proposed method is based on the following reparametrization $\{\sqrt{\gamma}\mathbf{w}_j \cdot \mathbf{x}\} \rightarrow \{\sqrt{\gamma}\boldsymbol{\theta}_j \cdot \mathbf{x}\}$, where $\{\mathbf{w}_j\}, \{\boldsymbol{\theta}_j\}_{j=1, \dots, d-1} \in \mathbb{R}^D$.

We illustrate the proposed method starting from base cases starting with the method to prepare the state $|\psi(\mathbf{x})\rangle_2 = \sqrt{\frac{1}{4}} [1, e^{i\sqrt{\gamma}\mathbf{w}_1 \cdot \mathbf{x}}, e^{i\sqrt{\gamma}\mathbf{w}_2 \cdot \mathbf{x}}, e^{i\sqrt{\gamma}\mathbf{w}_3 \cdot \mathbf{x}}]$ that corresponds to 2 qubits, 4 QAFF and the classical feature $\mathbf{x} \in \mathbb{R}^D$. The method starts by applying a single Hadamard gate to each qubit, followed by rotations $R_z(\sqrt{\gamma}\boldsymbol{\theta}_1 \cdot \mathbf{x})$ in the first qubit and $R_z(\sqrt{\gamma}\boldsymbol{\theta}_2 \cdot \mathbf{x})$ in the second qubit. We then apply a CNOT gate which controls the first qubit and targets the second qubit followed by a last rotation $R_z(\sqrt{\gamma}\boldsymbol{\theta}_3 \cdot \mathbf{x})$ on the second qubit as show in the Fig. 9a. These operations create the state $|\psi(\mathbf{x})\rangle_2 = \sqrt{\frac{1}{4}} [1, e^{i\sqrt{\gamma}(\boldsymbol{\theta}_1 + \boldsymbol{\theta}_2) \cdot \mathbf{x}}, e^{i\sqrt{\gamma}(\boldsymbol{\theta}_2 + \boldsymbol{\theta}_3) \cdot \mathbf{x}}, e^{i\sqrt{\gamma}(\boldsymbol{\theta}_1 + \boldsymbol{\theta}_3) \cdot \mathbf{x}}]'$. The structure of this quantum state preparation for two qubits has been explored in Ref. [75] in the context of amplitude encoding. The desired quantum Fourier map is obtained by setting the parameters $\{\boldsymbol{\theta}_j\}$ such that $\boldsymbol{\theta}_1 + \boldsymbol{\theta}_2 = \mathbf{w}_1$, $\boldsymbol{\theta}_2 + \boldsymbol{\theta}_3 = \mathbf{w}_2$, and $\boldsymbol{\theta}_1 + \boldsymbol{\theta}_3 = \mathbf{w}_3$.

It is also possible to rewrite the previous state preparation by defining the operations $C_1^{0 \rightarrow 1}$ and $C_2^{1 \rightarrow 2}$ as controlled rotations in the z axis, where the subindex indicates the number of qubits involved in the operation, and the superindex indicates the controlled qubits followed by an arrow to the single target qubit, with the top qubit of the circuit considered as the qubit 1, and the zero index indicating no controlled qubit. The two-qubit state preparation can be realized by applying a H gate to each qubit followed by the $C_1^{0 \rightarrow 1}$ operation in the first qubit corresponding to a R_z rotation, followed by the $C_2^{1 \rightarrow 2}$, which is built by grouping the two single R_z rotations in the second qubit with the CNOT, as shown in Fig. 9a.

We now illustrate the quantum state preparation for eight quantum Fourier features and three qubits with single R_z qubit rotations with angles $\{\sqrt{\gamma}\boldsymbol{\theta}_j \cdot \mathbf{x}\}_{j=1, \dots, 7}$. First, we apply a Hadamard gate to each of the three qubits, and then the preparation of the first two qubits corresponds to the previous two-qubit state preparation, i.e., we apply the operations $C_1^{0 \rightarrow 1}$, and $C_2^{1 \rightarrow 2}$, and then we apply twice the operation $C_2^{1 \rightarrow 3}$ that shares the same structure of $C_2^{1 \rightarrow 2}$; the CNOT has the same control qubit (first qubit), but it changes the R_z rotations and the target of the CNOT from qubit 2 to qubit 3. Hence, we apply twice $C_2^{1 \rightarrow 3}$ with different angular rotations in the z basis as shown in Fig. 9b and then we connect these operations with a CNOT which controls the second qubit and targets the third qubit, creating the state,

$$|\psi(\mathbf{x})\rangle_3 = \sqrt{\frac{1}{8}} \exp \left(i\sqrt{\gamma} [0, \boldsymbol{\Theta}_{1,2,5,6} \cdot \mathbf{x}, \boldsymbol{\Theta}_{2,3,4,5} \cdot \mathbf{x}, \boldsymbol{\Theta}_{1,3,4,6} \cdot \mathbf{x}, \boldsymbol{\Theta}_{4,5,6,7} \cdot \mathbf{x}, \boldsymbol{\Theta}_{1,2,4,7} \cdot \mathbf{x}, \boldsymbol{\Theta}_{2,3,6,7} \cdot \mathbf{x}, \boldsymbol{\Theta}_{1,3,5,7} \cdot \mathbf{x}]' \right), \quad (\text{A2})$$

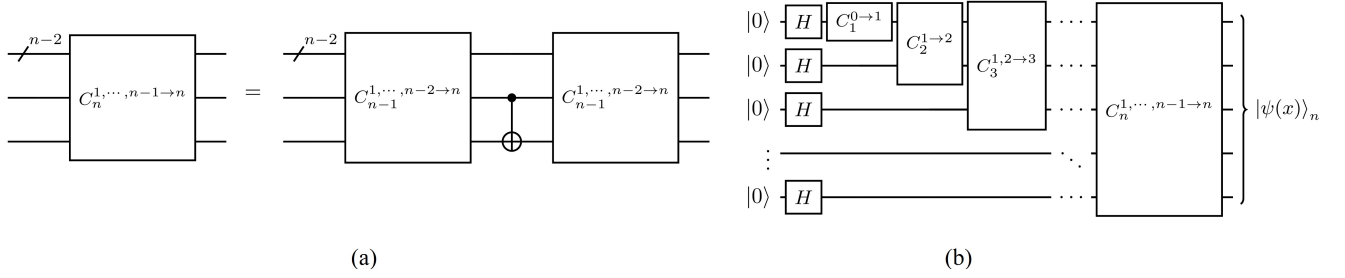


FIG. 10. Recursive construction of the quantum adaptive Fourier features on n qubits, (a) shows the construction of the operator $C_n^{1, \dots, n-1 \to n}$ as the concatenation of two operators $C_{n-1}^{1, \dots, n-2 \to n}$ and a CNOT gate in between which controls the $(n-1)$ th qubit and targets the (n) th qubit, and (b) shows the construction of the total QAFF circuit for an arbitrary number of qubits n in terms of these recursive operators.

where we define $\Theta_{r,s,t,u} = (\theta_r + \theta_s + \theta_t + \theta_u)$, and we set the corresponding parameters equal to the corresponding weights $\{\mathbf{w}_j\}_{j=1, \dots, 7}$ that build the QAFF with three qubits.

We may generalize these previous state preparation strategies by defining recursively the operation $C_n^{1, \dots, n-1 \to n}$, which corresponds to a transformation on n qubits with controls the first $n-1$ qubits and target the n^{th} qubit. This operation is defined by considering the previous case $C_{n-1}^{1, \dots, n-2 \to n-1}$ whose target is the $(n-1)^{\text{th}}$ qubit. We may construct an equivalent operation $C_{n-1}^{1, \dots, n-2 \to n}$ that shares the same sequence of gates as the $C_{n-1}^{1, \dots, n-2 \to n-1}$, namely, both share the same control qubits for the CNOTs, but the R_z rotations and targets of the CNOTs move from the $(n-1)^{\text{th}}$ qubit to the n^{th} qubit. Then, we construct recursively $C_n^{1, \dots, n-1 \to n}$, by applying twice $C_{n-1}^{1, \dots, n-2 \to n}$ on the n qubits, each duplicate with distinct R_z rotation angles and connecting these two duplicates with a CNOT which controls the $(n-1)$ th qubit and targets the n th qubit as shown in Fig. 10a. To further illustrate the method, Fig. 9c shows the $C_4^{1,2,3 \to 4}$ case which is defined from $C_3^{1,2 \to 3}$ (Fig. 9b).

Based on the transformations $\{C_i^{1, \dots, i-1 \to i}\}$, we may construct an ansatz for QAFF that also corresponds to an arbitrary quantum state preparation in the z basis on n qubits, by first applying a H gate to each of the n qubits followed by the $C_1^{0 \to 1}$, $C_2^{1 \to 2}$, $C_3^{1,2 \to 3}$, $C_4^{1,2,3 \to 4}$, \dots , $C_n^{1, \dots, n-1 \to n}$. The final quantum state $|\psi(\mathbf{x})\rangle_n$ will be given by,

$$|\psi(\mathbf{x})\rangle_n = \left[\prod_{i=1}^n (C_{n-i+1}^{1, \dots, n-i \to n-i+1} \otimes I_{i-1}) \right] H_n |0\rangle_n, \quad (\text{A3})$$

where we define $I_{i-1} = I^{\otimes i-1}$ as the identity matrix for $i-1$ qubits, and $H_n = H^{\otimes n}$ to the n initial Hadamard gates applied to each qubit. Also, each $C_i^{1, \dots, i-1 \to i}$ is composed of 2^{i-1} rotations from the set $\{R_z(\sqrt{\gamma}\theta_j \cdot \mathbf{x})\}$ and $2^{i-1} - 1$ CNOT gates. The depth of the QAFF ansatz (total number of CNOTs) is given by $\sum_{i=1}^n (2^{i-1} - 1) = 2^n - (n+1)$, and it requires $\sum_{i=1}^n 2^{i-1} = 2^n - 1$ R_z rotations, which match the number of independent phase variables of an arbitrary pure state on n qubits.

As stated before, this recursive method can also be used to build an ansatz for an arbitrary pure quantum state on n qubits. To build an arbitrary state in the z basis, we apply the same ansatz as the QAFF (which starts by applying H_n to the $|0\rangle_n$ state), but replace the single-qubit rotations $\{R_z(\sqrt{\gamma}\theta_j \cdot \mathbf{x})\}_{j=1, \dots, d-1}$ with the rotations $\{R_z(\delta_j)\}_{j=1, \dots, d-1}$, where the $\{\delta_j\}$ depend on the phases of the pure state to be learned or to be prepared and $d = 2^n$. We can also build a pure quantum state with only real components by ignoring the H_n operation, and applying the sequence of $\{C_i^{1, \dots, i-1 \to i}\}$ to the $|0\rangle_n$ state with R_y rotations instead of R_z rotations. Furthermore, the QAFF ansatz can be used to prepare an arbitrary complex-valued quantum state of n qubits by first building a pure state with real components with the R_y rotations followed by the R_z rotations to account for the phases of the complex components. Compared to a common mechanism for building quantum states such as the presented in Ref. [58], our method uses fewer CNOT gates for the preparation of arbitrary quantum states in either the y basis or in the z basis, but has the same depth and structure when combining both y and z rotations to build arbitrary quantum states.

Considering that the depth of the QAFF map $|\psi(\mathbf{x})\rangle_n$ (number of CNOTs) is $2^n - (n+1) = d - (\log d - 1)$, which is independent on the size D of the original data, this mapping can represent high-dimensional data in quantum computers with a low number of qubits. Furthermore, the complexity of the QAFF method for estimating the Gaussian kernel with the projection $|\langle \psi(\mathbf{x}_l) | \psi(\mathbf{x}_m) \rangle|^2$ is $O(TDd + TdR)$ where T is the number of data pairs $\{(\mathbf{x}_l, \mathbf{x}_m)\}$, and R is the total number of $|0\rangle_n$ measurements required to estimate $\hat{k}_{\{\mathbf{w}_j\}}(\mathbf{x}_l, \mathbf{x}_m) = |\langle \psi(\mathbf{x}_l) | \psi(\mathbf{x}_m) \rangle|^2$ with the quantum kernel estimation algorithm [60]; this result follows from the fact that for each data pair $(\mathbf{x}_l, \mathbf{x}_m)$ it is required $O(Dd)$ steps to find the angles $\{\sqrt{\gamma}\theta_j \cdot \mathbf{x}\}$, $O(d)$ to prepare the QAFF states and R measurement shots to estimate the

projection. In Appendix B, we illustrate the overall quantum complexity of training QAFF by taking into account the gradients of the method.

Appendix B: Gradients and complexity of the classical and quantum QAFF

In this section, we illustrate how to find the gradients of the loss function $\mathcal{L}_{\{\mathbf{w}_k\}}$ that depends on the operation $\hat{k}_{\{\mathbf{w}_k\}}(\mathbf{x}_l, \mathbf{x}_m) = |\langle \psi(\mathbf{x}_l) | \psi(\mathbf{x}_m) \rangle|^2$ for the QAFF, see Eqs. 9 and 11, in both classical and quantum computers.

The gradient of the loss function $\mathcal{L}_{\{\mathbf{w}_k\}}$ with respect to some \mathbf{w}_j may be written as,

$$\nabla_{\mathbf{w}_j} \mathcal{L}_{\{\mathbf{w}_k\}} = \frac{1}{N^2} \sum_{l=1}^N \sum_{m=1}^N \left[-2(k(\mathbf{x}_l, \mathbf{x}_m) - |\langle \psi(\mathbf{x}_l) | \psi(\mathbf{x}_m) \rangle|^2) \nabla_{\mathbf{w}_j} (|\langle \psi(\mathbf{x}_l) | \psi(\mathbf{x}_m) \rangle|^2) \right], \quad (\text{B1})$$

where $\nabla_{\mathbf{w}_j} (|\langle \psi(\mathbf{x}_l) | \psi(\mathbf{x}_m) \rangle|^2)$ may be written explicitly as,

$$\begin{aligned} \nabla_{\mathbf{w}_j} \left[\left(\sum_{k=0}^{d-1} \frac{1}{d} e^{i\sqrt{\gamma} \mathbf{w}_k \cdot (\mathbf{x}_l - \mathbf{x}_m)} \right) \left(\sum_{k=0}^{d-1} \frac{1}{d} e^{-i\sqrt{\gamma} \mathbf{w}_k \cdot (\mathbf{x}_l - \mathbf{x}_m)} \right) \right] = \\ \frac{1}{d} (i\sqrt{\gamma}(\mathbf{x}_l - \mathbf{x}_m)) \left[e^{i\sqrt{\gamma} \mathbf{w}_j \cdot (\mathbf{x}_l - \mathbf{x}_m)} \langle \psi(\mathbf{x}_l) | \psi(\mathbf{x}_m) \rangle - e^{-i\sqrt{\gamma} \mathbf{w}_j \cdot (\mathbf{x}_l - \mathbf{x}_m)} \langle \psi(\mathbf{x}_m) | \psi(\mathbf{x}_l) \rangle \right]. \end{aligned} \quad (\text{B2})$$

Based on the previous equation, for each data pair, these d gradients can be calculated on a classical computer with complexity $O(Dd + d^2)$, therefore the total complexity of training classically QAFF is $O(TDd + Td^2)$.

To build this operation in a quantum computer we may use parameter-shift rule [61], by shifting the parameter $(\sqrt{\gamma} \mathbf{w}_j \cdot (\mathbf{x}_l - \mathbf{x}_m))$ of $|\langle \psi(\mathbf{x}_l) | \psi(\mathbf{x}_m) \rangle|^2$ to $(\sqrt{\gamma} \mathbf{w}_j \cdot (\mathbf{x}_l - \mathbf{x}_m) + \pi/2)$ and $(\sqrt{\gamma} \mathbf{w}_j \cdot (\mathbf{x}_l - \mathbf{x}_m) - \pi/2)$, since $|\langle \psi(\mathbf{x}_l) | \psi(\mathbf{x}_m) \rangle|^2$ might be written as $\langle x | U^\dagger(\sqrt{\gamma} \mathbf{w}_j \cdot (\mathbf{x}_l - \mathbf{x}_m)) \hat{B} U(\sqrt{\gamma} \mathbf{w}_j \cdot (\mathbf{x}_l - \mathbf{x}_m)) | x \rangle$, for some state $|x\rangle$ and some operator \hat{B} on n qubits that do not depend on \mathbf{w}_j . Hence from parameter-shift rule the gradient can also be computed by,

$$\begin{aligned} \nabla_{\mathbf{w}_j} (|\langle \psi(\mathbf{x}_l) | \psi(\mathbf{x}_m) \rangle|^2) &= \frac{1}{2} \sqrt{\gamma}(\mathbf{x}_l - \mathbf{x}_m) \left[\langle x | U^\dagger(\sqrt{\gamma} \mathbf{w}_j \cdot (\mathbf{x}_l - \mathbf{x}_m) + \pi/2) \hat{B} U(\sqrt{\gamma} \mathbf{w}_j \cdot (\mathbf{x}_l - \mathbf{x}_m) + \pi/2) | x \rangle \right. \\ &\quad \left. - \langle x | U^\dagger(\sqrt{\gamma} \mathbf{w}_j \cdot (\mathbf{x}_l - \mathbf{x}_m) - \pi/2) \hat{B} U(\sqrt{\gamma} \mathbf{w}_j \cdot (\mathbf{x}_l - \mathbf{x}_m) - \pi/2) | x \rangle \right] = \\ &\frac{1}{2} \sqrt{\gamma}(\mathbf{x}_l - \mathbf{x}_m) \left[|\langle \psi(\mathbf{x}_l) | \psi(\mathbf{x}_m) \rangle|^2_{\sqrt{\gamma} \mathbf{w}_j \cdot (\mathbf{x}_l - \mathbf{x}_m) \rightarrow \sqrt{\gamma} \mathbf{w}_j \cdot (\mathbf{x}_l - \mathbf{x}_m) + \pi/2} - |\langle \psi(\mathbf{x}_l) | \psi(\mathbf{x}_m) \rangle|^2_{\sqrt{\gamma} \mathbf{w}_j \cdot (\mathbf{x}_l - \mathbf{x}_m) \rightarrow \sqrt{\gamma} \mathbf{w}_j \cdot (\mathbf{x}_l - \mathbf{x}_m) - \pi/2} \right], \end{aligned}$$

where in the last line the arrow in the subindex indicates the applied parameter-shift rule. Hence, we may use the QAFF mapping along with the kernel estimation algorithm [60] to estimate the gradients of the QAFF. Although, in this argument we parameterized the QAFF by $\{\sqrt{\gamma} \mathbf{w}_j \cdot \mathbf{x}\}$ which correspond to uniformly controlled R_z rotations as explained in Sect. IV B 2, we can also apply an equivalent parameter-shift rule to the QAFF reparameterized with single R_z rotations with angles $\{\sqrt{\gamma} \theta_j \cdot \mathbf{x}\}$, see Appendix A.

Knowing the gradients of the loss function is sufficient to optimize the weights of the QAFF hence the total quantum complexity of QAFF lies on estimating these gradients, see Eq. B1. In Appendix A, we showed that to estimate $|\langle \psi(\mathbf{x}_l) | \psi(\mathbf{x}_m) \rangle|^2$ it is required $O(TDd + TdR)$ where D is the size of the classical data, d is the number of Fourier features, T is the number of data pairs $\{(\mathbf{x}_l, \mathbf{x}_m)\}$, and R is the number of $|0\rangle_n$ measurements of the quantum kernel estimation circuit. The estimation of the gradients $\nabla_{\mathbf{w}_j} (|\langle \psi(\mathbf{x}_l) | \psi(\mathbf{x}_m) \rangle|^2)$ accounts for an additional quantum complexity of $O(Td^2R)$ considering that for each of the d Fourier vector weights $\{\mathbf{w}_j\}$ (or $\{\theta_j\}$) and each data pair $(\mathbf{x}_l, \mathbf{x}_m)$ we need to find its gradient by estimating the projection $|\langle \psi(\mathbf{x}_l) | \psi(\mathbf{x}_m) \rangle|^2$ with shifted parameter $\mathbf{w}_j \cdot (\mathbf{x}_l - \mathbf{x}_m)$ with complexity $O(dR)$, because we only recalculate the angles $\{\sqrt{\gamma} \mathbf{w}_j \cdot \mathbf{x}\}$ when doing the gradient estimation of a different data pair. Therefore, the overall quantum complexity to train the QAFF corresponds to $O(TDd + Td^2R)$. Furthermore, the complexity of extracting the quantum Fourier features of a data set with N samples is $O(Nd + Nd \log dR)$, because for each data sample, it is required $O(Dd)$ to find the Fourier angles of the QAFF, and $O(d \log dR)$ to prepare the d Fourier components and to measure R times the $n = \log d$ bit strings that form the basis.

Appendix C: SDM ansatz, density matrix preparation from eigenbasis

The SDM (spectral density matrix) ansatz to initialize a density matrix $\rho \in \mathbb{C}^{d \times d}$ with rank r departing from its spectral decomposition requires $n + m$ qubits, such that $n = \lceil \log(d) \rceil$, and $m = \lceil \log(r) \rceil$. Let $\rho = U \Lambda U^\dagger$ be the

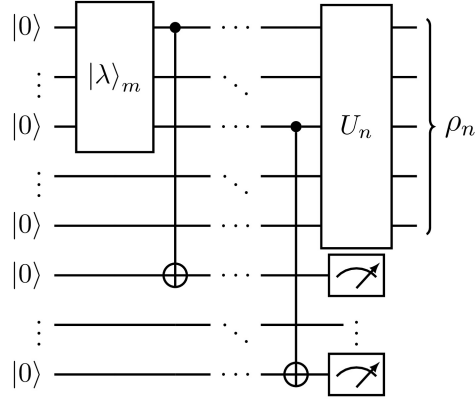


FIG. 11. SDM ansatz: mixed state preparation from its spectral decomposition. Considering the eigendecomposition of the density matrix $\rho = U\Lambda U^\dagger$, we prepare Λ with an entangled state between the first m qubits and the last m qubits and U with an isometry in the first n qubits.

spectral decomposition of the density matrix, where U is a unitary matrix whose first r columns are the eigenvectors of ρ and $\Lambda = [\sum_{i=0}^{r-1} \lambda_i |i\rangle\langle i| + \sum_{i=r}^{d-1} 0 |i\rangle\langle i|]$ is the diagonal matrix of eigenvalues. The protocol begins by initializing the first m qubits with the state $|\lambda\rangle_m = \sum_{i=0}^{r-1} \sqrt{\lambda_i} |i\rangle_m$, thanks to amplitude encoding [58, 59]. Therefore, the circuit starts with the state,

$$\sum_{i=0}^{r-1} \sqrt{\lambda_i} |i\rangle_m \otimes |0\rangle_{(n-m)} \otimes |0\rangle_m, \quad (\text{C1})$$

then, a cascade of m CNOT gates between the first m qubits and the last m qubits are applied to the circuit, as shown in Fig. 11. The j^{th} CNOT controls the j^{th} qubit and targets the $(n+j)^{\text{th}}$ qubit for $j \in \{0, \dots, m-1\}$. The resulting quantum state of this operation is,

$$\sum_{i=0}^{r-1} \sqrt{\lambda_i} |i\rangle_m \otimes |0\rangle_{(n-m)} \otimes |i\rangle_m, \quad (\text{C2})$$

followed by a partial trace on the purification by performing a measurement on the last m qubits, which results in a mixed state in the first m qubits with only classical probability,

$$\Lambda_n = \left(\sum_{i=0}^{r-1} \lambda_i |i\rangle\langle i|_m \right) \otimes |0\rangle\langle 0|_{n-m}. \quad (\text{C3})$$

The desired density matrix is obtained by applying to the state Λ_n an isometry [57] U_n from m qubits to n qubits, given by,

$$U_n = \begin{pmatrix} U & 0 \\ 0 & I \end{pmatrix}, \quad (\text{C4})$$

which prepares the r eigenvectors of ρ in the first r columns of U_n and I is the identity matrix with rank $2^n - d$, the process results in the desired mixed state,

$$\rho_n = U_n \Lambda_n U_n^\dagger. \quad (\text{C5})$$

as shown in Fig 11. Note that measuring the last m qubits after applying the isometry U_n leads to the same result.

The mixed state preparation protocol from its spectral decomposition was first proposed in qudit-based quantum computers [19], here we extend the method to quantum computers based on qubits. After the initial version of this manuscript, an independent work on the preparation of mixed states with qubits was released [76], applied to the problem of mixed state learning.

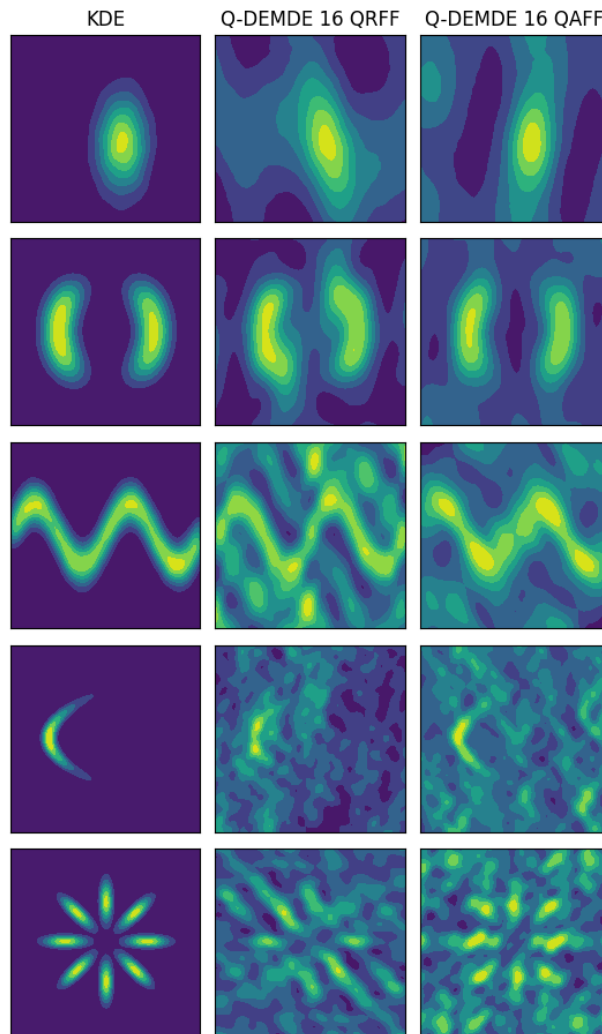


FIG. 12. Two-dimensional quantum-classical density estimation with the proposed Q-DEMDE algorithm with 16 Fourier components for both QRFF and QAFF. In contrast to the results of Sect. VB, which use classical hardware to train the QAFF, here, we present the results of using a PennyLane noiseless quantum simulator to optimize the Fourier features. From top to bottom, the two-dimensional data sets correspond to Binomial, Potential 1, Potential 2, Arc, and Star Eight.

Appendix D: Additional simulations for hybrid 2-D density estimation with quantum variational QAFF

Although the hybrid density estimation method Q-DEMDE uses classical computers to train the quantum adaptive Fourier features, in this section, we demonstrate the feasibility of using a quantum simulator to learn the quantum adaptive Fourier features for density estimation via the quantum variational algorithm described in Sect. IV B 2.

1. Setup

We present the results for 2-dimensional density estimation using the Q-DEMDE algorithm with the QAFF learned in a PennyLane noiseless quantum simulator. Similar to the simulations of Sect. VB, we tested the algorithm on five 2-dimensional density estimation data sets: Binomial, Potential 1, Potential 2, Arc, and Star, shown from top to bottom in Fig. 12. The training points corresponded to 10000 points sampled from these distributions, and the test samples, whose probability density we wanted to estimate, were the result of dividing the space of each 2D data set into a grid of 120×120 points.

We used the quantum variational strategy described in Sect. IV B 2 and Appendix A to train the quantum adaptive Fourier features in a noiseless quantum simulator of the PennyLane python library [68]. In total, we trained 16 adaptive

Fourier features, requiring a quantum circuit of 4 qubits and $15 \times 2 = 30$ variational parameters, corresponding to 15 Fourier vector weights $\{\theta_j\} \in \mathbb{R}^2$, using the QAFF mapping described in the Appendix A. For each 2D density estimation data set, we initialized the adaptive Fourier weights from $U[0, 1]$, and used these 2-dimensional data sets as the kernel training data sets, see Sect. IV B 1. After learning the optimal Fourier weights, $\{\theta_j\}$, we prepared the QAFF mappings of the training and test density estimation data samples by making predictions from the QAFF quantum circuit. Once the QAFF were prepared, we followed the steps of the main Q-DEMDE method, i.e., we constructed the 16×16 training density matrix, computed its spectral decomposition with 16 eigenvalues, and estimated the density estimation of the test samples using the 8-qubit Q-DMKDE quantum algorithm with the PennyLane quantum simulator.

We evaluated the hybrid Q-DEMDE with quantum variational QAFF by comparing the obtained probability density values with the probability densities obtained with KDE [14, 15], using the density estimation metrics KL-Div, MAE, and Spearman correlation. As a baseline, we also performed hybrid density estimation using the Q-DEMDE method with 16 QRFF.

2. Results and discussion

We present the results of the Q-DEMDE density estimation method with quantum variational QAFF in Fig. 12 and Table X. The results of the simulations show that it is possible to perform quantum-classical density estimation by learning the QAFF feature map in a quantum simulator, for instance, the QDE method achieved satisfactory results for density estimation, especially on the Potential 2 data set; it is worth highlighting that the adaptive Fourier weights were randomly initialized from $U[0, 1]$, thus the method was able to capture the optimal Fourier parameters. However, the results also show better performance of the Q-DEMDE method with QRFF on the Binomial, Potential 1, Arc and Star data sets, indicating that the results of Q-DEMDE method could have been improved by increasing the number of training iterations and using the Gaussian kernel training data set, see Sect. IV B 1, which is to be explored in future work.

Although the primary Q-DEMDE strategy uses classical computers to prepare the QAFF, it is worth reemphasizing, as in Sect. VB 3, that learning the Gaussian kernel with QAFF in quantum hardware could have applications to other quantum machine learning algorithms that do not require performing intermediate classical computations.

Data Set	Metric	Q-DEMDE 16 QRFF	Q-DEMDE 16 QAFF
Binomial	KL-Div	0.795	1.053
	MAE	0.029	0.073
	Spearman	0.573	0.283
Potential 1	KL-Div	0.639	0.631
	MAE	0.079	0.079
	Spearman	0.803	0.539
Potential 2	KL-Div	1.050	0.929
	MAE	0.316	0.330
	Spearman	0.389	0.538
Arc	KL-Div	2.040	2.431
	MAE	0.017	0.040
	Spearman	0.218	-0.027
Star Eight	KL-Div	1.383	1.433
	MAE	0.162	0.156
	Spearman	0.325	0.119

TABLE X. 2D quantum-classical density estimation results with Q-DEMDE algorithm with 16 Fourier components for both QRFF and QAFF. The QAFF were trained using a PennyLane noiseless quantum simulator. The best results are shown in bold.

Appendix E: Description of the IBM-Oslo quantum device

All the demonstrations related to applications of the methods presented in this paper on real quantum systems were performed on the IBM-Oslo quantum computer, one of the quantum processors made publicly available through the IBM Quantum Platform. The layout of the quantum processor is shown in Fig. 13, and other relevant features of the processor are listed in Table XI.

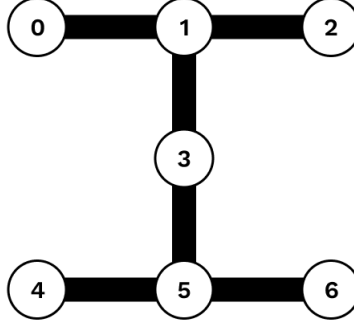


FIG. 13. Topological map of the IBM-Oslo quantum processor.

CLOPS (Circuit layer operations per second)	2.6K
Median fundamental transition frequency	5.046 GHz
Median anharmonicity	-0.3429 GHz
Median qubit lifetime T_1	128 μ s
Median coherence time T_2	79.89 μ s
Single qubit gate error	1.65×10^{-4} to 6.698×10^{-4}
CNOT gate error	6.47×10^{-3} to 2.067×10^{-2}
Average readout error	0.0216

TABLE XI. Main features of the IBM-Oslo quantum processor. The IBM-Oslo parameters were taken from Ref. [77].

Appendix F: Two-dimensional data sets

We used five synthetic two-dimensional data sets from Ref. [67] to evaluate our proposed quantum density estimation method. The data sets are characterized as follows:

- *Binomial* data set corresponds to a two-dimensional random sample drawn from the random vector $\mathbf{X} = (X_1, X_2)$ with a probability density function given by multinomial distribution $\mathcal{N}(\mathbf{x}|\boldsymbol{\mu}_1, \boldsymbol{\Sigma}_1)$ with mean $\boldsymbol{\mu}_1 = [1, -1]^T$ and covariance matrix $\boldsymbol{\Sigma}_1 = \begin{bmatrix} 1 & 0 \\ 0 & 2 \end{bmatrix}$.

- *Potential 1* data set corresponds to a two-dimensional random sample drawn from a random vector $\mathbf{X} = (X_1, X_2)$ with probability density function given by

$$f(\mathbf{x}_1, \mathbf{x}_2) = \frac{1}{2} \left(\frac{\|\mathbf{x}\| - 2}{0.4} \right)^2 - \ln \left(\exp \left\{ -\frac{1}{2} \left[\frac{\mathbf{x}_1 - 2}{0.6} \right]^2 \right\} + \exp \left\{ -\frac{1}{2} \left[\frac{\mathbf{x}_2 + 2}{0.6} \right]^2 \right\} \right)$$

with a normalizing constant of approximately 6.52 calculated by Monte Carlo integration.

- *Potential 2* data set corresponds to a two-dimensional random sample drawn from a random vector $\mathbf{X} = (X_1, X_2)$ with probability density function given by

$$f(\mathbf{x}_1, \mathbf{x}_2) = \frac{1}{2} \left[\frac{\mathbf{x}_2 - w_1(\mathbf{x})}{0.4} \right]^2$$

where $w_1(\mathbf{x}) = \sin\left(\frac{2\pi x_1}{4}\right)$ with a normalizing constant of approximately 8 calculated by Monte Carlo integration.

- *Arc* data set corresponds to a two-dimensional random sample drawn from a random vector $\mathbf{X} = (X_1, X_2)$ with probability density function given by

$$f(\mathbf{x}_1, \mathbf{x}_2) = \mathcal{N}(\mathbf{x}_2|0, 4)\mathcal{N}(\mathbf{x}_1|0.25\mathbf{x}_2^2, 1)$$

where $\mathcal{N}(u|\mu, \sigma^2)$ denotes the density function of a normal distribution with mean μ and variance σ^2 .

- *Star Eight* data set corresponds to a two-dimensional random sample drawn from a random vector $\mathbf{X} = (X_1, X_2)$. The bivariate probability distribution function is generated from a Gaussian bivariate random variable \mathbf{z} as

$$f(\mathbf{x}_1, \mathbf{x}_2) = -\ln \left(e^{-\frac{1}{2} \left[\frac{\mathbf{z}_2 - w_1(\mathbf{z})}{0.35} \right]^2} + e^{-\frac{1}{2} \left[\frac{\mathbf{z}_2 - w_1(\mathbf{z}) + w_2(\mathbf{z})}{0.35} \right]^2} \right)$$

where $w_1(\mathbf{z}) = \sin\left(\frac{2\pi\mathbf{z}}{4}\right)$ and $w_2(\mathbf{z}) = 3e^{-\frac{1}{2} \left[\frac{\mathbf{z}-1}{0.6} \right]^2}$.